

# A MODEL STUDY OF MOLECULAR TRANSPORT IN ELECTROPORATION

BY MIAO YU

A dissertation submitted to the  
Graduate School—New Brunswick  
Rutgers, The State University of New Jersey  
in partial fulfillment of the requirements  
for the degree of  
Doctor of Philosophy  
Graduate Program in Mechanical and Aerospace Engineering

Written under the direction of  
Professor Hao Lin  
and approved by

---

---

---

---

New Brunswick, New Jersey

October, 2014

## ABSTRACT OF THE DISSERTATION

### A model study of molecular transport in electroporation

by Miao Yu

Dissertation Director: Professor Hao Lin

Reversible electroporation is a non-viral technique to introduce foreign molecules into biological cells or tissues, which has found applications in fields including gene transfer, cancer treatment, stem-cell research etc. Despite its promising potential, the improvement of electroporation technique is impeded by the lack of a comprehensive understanding of the underlying mechanisms involved in the process of molecular delivery. This work aims at implementing model studies of electroporation-mediated molecular delivery with the target varying from small molecules (propidium iodide, PI) to macromolecules (DNA). Three significant tasks have been accomplished. First, a model study is performed on the electroporation-mediated delivery of PI. In particular, the effects of extra-cellular conductivity on the amount of PI delivery are carefully investigated and discussed. The results are extensively compared with experiments by Sadik *et al.* [72], and reveal important physical insights about the transport mechanisms involved. It is confirmed that the electrophoretic transport, not the diffusive transport, is the dominating mechanism in mediating PI delivery, and the inverse correlation observed between PI delivery and extra-cellular conductivity results from an electrokinetic phenomenon termed Field Amplified Sample Stacking (FASS). Second, a model investigation of Fluorescein-Dextran delivery is implemented for double-pulse electroporation.

Simulated results find qualitative agreement with experiments in predicting the correlation between delivery and pulsing parameters. A bifurcation analysis of equilibrium pore size with respect to the transmembrane potential is presented to explain the observed critical field strength above which the second pulse abruptly becomes effective in mediating delivery. Third, a 1D Fokker-Planck simulation is used to characterize the process of DNA translocation through an electropore under finite DC pulses. It is found that the translocation may occur on two disparate time scales, the electrophoretic time ( $\sim$  ms), and the diffusive time ( $\sim$  s), depending on the pulse length. Furthermore, a power-law correlation is observed between the final probability of successful translocation and pulsing parameters. Simulated results are compared with previous data to interpret the trends, and further model predictions are made which can be verified by well-designed experiments. Together, these projects establish connections between available theoretical model and experimental observations in electroporation research. Such a connection on one hand benefits experimentalists in providing a powerful prediction tool for the design and optimization of electroporation; on the other hand it equally benefits theorists to improve the models and advance fundamental understandings in the subject.

## Acknowledgements

First and foremost, I would like to express my sincere gratitude to my advisor, Prof. Hao Lin for his continuous support of my PhD study and research. This dissertation is accomplished with his guidance in every aspect. It is his enthusiasm, professionalism and unremitting pursuit of high-quality work that always push me forward to improve myself in academics. It is his tolerance, patience and consideration that has helped me overcome the difficulties during my PhD program. He has been a mentor of not only my academic life, but also my real life. It is truly a fortune for me to have him as my PhD advisor.

I am grateful to my collaborators, Prof. Jerry W. Shan, Prof. David I. Shreiber, Prof. Jeffrey. D. Zahn, Prof. Jingang Yi and Prof. Liping Liu at Rutgers University for their helpful suggestions and discussions. I would like to thank Prof. Prosenjit Bagchi at Rutgers University for being my committee member and his valuable suggestions in my defense.

I would like to thank my senior colleague Jianbo Li for his consistent help and helpful discussions in eletroporation research, and especially for the numerical code provided to me ; Jia Zhang for his well-organized materials and fruitful communications on electrodeformation and relaxation research; Mohamed Sadik for sharing his experimental data and precious suggestions from a biological point of view. I would like to give special thanks to all my group members and friends in the United States for their support in the past years.

Finally, I would like to express my deepest gratitude to my parents, Chunsheng Yu and Yanbing Xiao for their support with love and wisdom throughout my life; my uncle and aunt, Yansong Xiao and Yan Chen, and all other family members for their considerations and blessings.

## Table of Contents

<b>Abstract</b> . . . . .	ii
<b>Acknowledgements</b> . . . . .	iv
<b>List of Tables</b> . . . . .	vii
<b>List of Figures</b> . . . . .	viii
<b>1. Introduction</b> . . . . .	1
<b>2. Propidium iodide delivery with millisecond electric pulses</b> . . . . .	5
2.1. Introduction . . . . .	5
2.2. Model formulation . . . . .	6
2.3. Results . . . . .	8
2.4. The equilibrium transmembrane potential . . . . .	17
2.5. Conclusions . . . . .	19
<b>3. Double-pulse electroporation</b> . . . . .	21
3.1. Introduction . . . . .	21
3.2. Summary of key observations . . . . .	22
3.3. Model formulation . . . . .	23
3.4. Results . . . . .	24
3.5. Conclusions . . . . .	27
<b>4. DNA translocation through an electropore</b> . . . . .	29
4.1. Introduction . . . . .	29
4.2. Model formulation . . . . .	31
4.3. Results . . . . .	34

4.4. Comparison with Experiments . . . . .	41
4.5. Conclusions . . . . .	45
<b>5. A preliminary study of vesicle/cell relaxation . . . . .</b>	<b>47</b>
5.1. Introduction . . . . .	47
5.2. A small-deformation analysis of vesicle relaxation . . . . .	48
5.2.1. Problem description . . . . .	48
5.2.2. The hydrodynamic problem . . . . .	50
5.2.3. Boundary conditions . . . . .	50
5.2.4. Base state . . . . .	51
5.2.5. Kinematic condition . . . . .	52
5.2.6. Results . . . . .	53
5.2.7. Discussion . . . . .	54
5.3. Extraction of membrane properties . . . . .	56
5.4. Conclusions . . . . .	57
<b>6. Conclusions . . . . .</b>	<b>60</b>
<b>Appendix A. Model formulation of electroporation-mediated delivery .</b>	<b>62</b>
A.1. The electrical problem . . . . .	62
A.2. Membrane permeabilization . . . . .	63
A.3. Species transport . . . . .	64
A.4. Numerical implementation . . . . .	66
<b>Appendix B. Supplements for Chapter 4 . . . . .</b>	<b>67</b>
<b>Appendix C. Supplements for Chapter 5 . . . . .</b>	<b>70</b>

## List of Tables

2.1. Definition of abbreviations. . . . .	6
2.2. List of model parameters in Chapter 2. . . . .	8
3.1. List of model parameters in Chapter 3. . . . .	24
4.1. Abbreviations used in Chapter 4 . . . . .	31
4.2. List of model parameters in Chapter 4 . . . . .	33

## List of Figures

2.1.	A schematic of the problem. $(r, \theta)$ denotes the spherical coordinate system. $x$ is the axis of rotation, and is aligned with the direction of field application. The field strength is denoted by $E_0$ . The intra- and extra-cellular conductivities are denoted by $\sigma_i$ and $\sigma_e$ , respectively. . . .	8
2.2.	Simulated membrane permeabilization under a single pulse of 0.8 kV/cm in strength and 100 ms in length, for various extra-cellular conductivities. (a) Evolution of the TMP, $V_m$ , at $\theta = \pi$ as a function of time. (b) Polar distribution of the TMP at $t = 95$ ms. (c) Evolution of local membrane conductance, $g_m$ , at $\theta = \pi$ as a function of time. (d) Membrane conductance at $\theta = 0, \pi$ at $t = 95$ ms. The dashed is a theoretical prediction, and the fitting constant $C = 1.46 \times 10^5$ S/m <sup>2</sup> . (e) Evolution of the PAD, $\rho_p$ , at $\theta = \pi$ as a function of time. (f) The PAD at $\theta = 0, \pi$ at $t = 95$ ms. . . . .	10
2.3.	Contour plots of convoluted PI concentration at the cell center-plane for $\sigma_e = 100$ $\mu$ S/cm (top) and 2000 $\mu$ S/cm (bottom). The snapshots are taken at $t=0, 20, 45, 70, 95, 121$ , and 4996 ms, following the experimental presentation in Sadik13. . . . .	11
2.4.	Species concentration evolution for $\sigma_e = 100$ $\mu$ S/cm and 2000 $\mu$ S/cm along the cell centerline, $x$ . . . . .	13
2.5.	(a) Evolution of integrated free PI and PIB concentrations over the entire cell ( $PI_{tot} + PIB_{tot}$ ) for the six values of $\sigma_e$ . The dashed vertical line indicates the end of the pulse. (b) Evolution of $PI_{tot} + PIB_{tot}$ during the pulse. (c) Evolution of integrated PIB concentration over the entire cell ( $PIB_{tot}$ ). (d) Evolution of $PIB_{tot}$ during the pulse. . . . .	14



- 2.6. Comparison of simulated results ('+', right axis) with experimental data from Sadik13 ('o', left axis). For the data, the middle and lower curves represent contributions to the total fluorescence intensity (TFI) during and after the pulse, respectively. The upper curve is the sum of the two. In comparison, numerical simulation of  $\text{PIB}_{\text{tot}}$  is presented, and the upper, middle, and lower curves are defined similarly. The right axis is scaled linearly such that the upper curves from data and simulation best match. (a) Simulated results using the original ASE model. The dotted line is a theoretical fitting with the functional form  $C/(2\sigma_e + \sigma_i)$ . (b) The size of the pores are artificially maintained for 1 s post-pulsation in the ASE model to allow for more diffusive delivery. . . . . 16
- 2.7. Schematics for the  $(r_{eq}, V_m)$  dynamics. (a) The relation between  $r_{eq}$  and  $V_m$  exhibits a pitchfork bifurcation behavior. Between  $V_m^{eq}$  and  $V_m^{crit}$ , three branches of solutions exist from Eq. (2.11), where the middle one (dash-dotted) is unstable. The initial charging and permeabilization process follows four stages denoted by I-IV. For this case  $\rho_p = 2 \times 10^{-3}$ . A detailed description is given in the text. (b) Exemplary evolution of  $V_m$  as a function of time. The stages I-IV correspond to those in (a). . . 18
- 3.1. Experimental results by Sadik *et al.* [73]. (a) The normalized Fluorescence (NF) of intracellular Fluorescein-Dextran as a function of  $t_2$ . Symbols represent experimental data; curves, least-square fitting corresponding to different cases ( $E_1$  varying between 10,000 and 100,000 V/m from bottom to top). (b) Measured delivery rate per unit time ( $\tau_f$ , circles) as a function of  $E_2$ . The error bars represent the 95% confidence interval of the fitting. The correlation between  $\tau_f$  and  $E_2$  can be further approximated by a least-square sigmoidal fitting (dashed). The coefficient of determination is  $R^2 = 0.97$ . . . . . 23
- 3.2. Simulated results of total delivery of Fluorescein-Dextran (TFD), plotted as a function of  $t_2$  for  $E_2$  varying between 10,000 and 100,000 V/m. . . 25

3.3.	Simulated results of delivery rate per unit time $\tau_f$ (the left axis) and the total permeabilized area (TPA, the right axis) plotted as a function of $E_2$ . $\tau_f$ is defined as the slopes of fitting lines in Fig. 3.2 corresponding to each value of $E_2$ . TPA is defined as the total area occupied by electropores on the cathode-facing hemisphere of the cell membrane. . . . .	26
3.4.	Evolution of the TPA during HV (0-1 ms) and at the beginning of LV (1-1.6 ms), with $E_2$ varying between 10,000 and 100,000 V/m. . . . .	27
4.1.	A schematic of the problem. The membrane is an infinitesimally thin plane separating region I (the extracellular space) and region II (the intracellular space). The electric potential in each region is denoted by $\Phi$ . . . . .	31
4.2.	Evolution of the PDF, $P(m, t)$ , for a DNA chain of $N = 24$ . The initial location is $m_0 = 0.2$ , the TMP is $V_m = 0.2$ V and the pulse length is $t_p = 5$ ms. In Fig. 4.2d, the PUT and the PST are indicated at the artificial nodes of $m = -1$ and 25, respectively. . . . .	35
4.3.	Evolution of the PDF, $P(m, t)$ , for a pulse length of $t_p = 20$ ms. All other parameters are identical to those used in Fig. 4.2. . . . .	35
4.4.	Evolution of the PST for the cases studied in Figs. 4.2 and 4.3. The end of the pulse is marked by dash-dotted lines. The final probability of successful translocation (F-PST) is defined as the value of the PST when it reaches the final steady state and is indicated. . . . .	36
4.5.	The F-PST as a function of the pulse length, $t_p$ , for $V_m = 0.2, 0.4$ , and 0.6 V. Other parameters are identical as those used in Fig. 4.2. . . . .	37
4.6.	Contour plot of the F-PST in the phase space of the TMP ( $V_m$ ) and the pulse length ( $t_p$ ). The slopes for the contour lines are approximately -1, indicating that $V_m \times t_p \approx \text{Constant}$ . . . . .	37

4.7.	The effect of DNA size on translocation probability. (a) The F-PST as a function of the DNA segment number, $N$ , for $t_p = 5, 10$ , and $20$ ms. The descending part of the curves follows approximately the correlation, $\text{F-PST} \sim N^{-1.5}$ . (b) Contour plot of the F-PST in the phase space of $N$ and $t_p$ . The contours are straight and parallel lines following the approximate correlation $N \sim t_p^{0.75}$ . . . . .	39
4.8.	The similarity behavior of the F-PST as a function of $V_m$ , $t_p$ , and $N$ . (a) $m_0 = 0.2$ . The squares represent simulated results for $V_m$ ranging from $0.1$ to $1$ V, $t_p$ from $0.01$ to $25$ ms, and $N$ from $17$ to $134$ . The solid line is a least-square fit, $\text{F-PST} = 45.0 \times (V_m t_p)^{1.10} / N^{1.46}$ . The coefficient of determination is $R^2 = 0.999$ . (b) The similarity behavior is also observed for $m_0 = 0.1, 0.5, 1$ , and $1.5$ . The simulation is run for the same parametric range as in Fig. 4.8a, and for $m_0 = 0.1, 0.5, 1$ , and $1.5$ , the collection of data is best-fitted with the correlation $\text{F-PST} = 60.0 \times (V_m t_p)^{1.07} / N^{1.51}$ (solid). The coefficient of determination is $R^2 = 0.946$ . . . . .	40
4.9.	Simulated F-PST as a function of $t_p$ using parameters found in Sukharev <i>et al.</i> [81]. The inset shows the original experimental data (stars) in terms of the TE measured by fluorescent intensity. . . . .	42
4.10.	(a) Experimental results from Faurie <i>et al.</i> [15]. The fluorescence intensity per viable cell is plotted as a function of the pulse repetition frequency. (b) Simulated result using parameters from the experiment. . . . .	43
5.1.	A schematic of the problem. . . . .	49

5.2.	Schematic of regimes in vesicle relaxation. Solid curves are numerical solution of Eq. (5.22) for two different values of membrane bending rigidity $\kappa$ . When the deformation is moderate ( $e > 1.2$ for this case), the aspect ratio shows a logarithm-like dependence on the dimensionless time $\tau$ . When the deformation is very small ( $e < 1.05$ ), the aspect ratio decays exponentially to 1 (spherical state), and the decaying time scale is independent of $\kappa$ (inset). There is a transition regime for $e$ between 1.05 and 1.2, which is not apparently seen in this case. . . . .	56
5.3.	Extraction of membrane bending rigidity $\kappa$ by fitting numerical solution (solid) of Eq. (5.22) and experimental data (symbols), for four different types of vesicles/cells. The vesicle/cell types are: POPC, vesicle of a lipid membrane of 1-palmitoyl-2-oleoyl-sn-glycero-3-phosphocholine; MCF7, a breast cancer cell line; Egg-PC GUV, Giant unilamellar vesicles of L- $\alpha$ -phosphatidylcholine from egg yolk; MDA-MB-231, a breast cancer cell line in metastatic state. . . . .	58
A.1.	A schematic of the problem. $(r, \theta)$ denotes the spherical coordinate system. $x$ is the axis of rotation, and is aligned with the direction of field application. The field strength is denoted by $E_0$ . The intra- and extra-cellular conductivities are denoted by $\sigma_i$ and $\sigma_e$ , respectively. . .	63
B.1.	Upon the completion of translocation, the center of mass translates by $2R_g$ , where $R_g$ is the radius of gyration. . . . .	68
B.2.	Simulated results with $\beta = 0.322$ , in comparison with the experimental data from Storm <i>et al.</i> [80]. The average translocation time $t_{tran}$ is plotted as a function of DNA size. The transmembrane potential is $V_m = 0.12$ V. The average translocation time is defined as the most probable time required for the DNA molecule to complete its translocation. . . .	69

# Chapter 1

## Introduction

The term "electroporation" or "electropermeabilization" refers to the phenomenon that a cell membrane becomes permeabilized when exposed under a strong enough external electric field [56]. Such permeabilization can be either irreversible or reversible. Irreversible electroporation often kills cells or damages their structure permanently, therefore it can be utilized to destroy tumors or ablate biological tissues in a drug-free manner. Irreversible electroporation has attracted increasing research interests recently, and become a promising tool in fields such as tissue ablation, debacterialization, and cancer therapy [53, 58, 70, 75]. Reversible electroporation provides an effective tool to introduce foreign molecules into biological cells while keeping their functionality, as those molecules in general cannot go through an intact cell membrane without the occurrence of membrane permeabilization. Reversible electroporation has found applications in gene delivery, cancer treatment, stem-cell research etc. [1, 7, 89, 46, 48, 57, 74, 88], and is the main focus of this thesis.

Compared to other chemical or biological techniques of molecular delivery, reversible electroporation is fast, safe, relatively cheap and easy to perform [13]. In addition, its effectiveness depends less on the cell type [22, 27]. Therefore it has become one of the most widespread techniques to transport molecules into organs and tissues. Nevertheless, the underlying mechanisms of electroporation-mediated molecular delivery are still relatively poorly understood [13]. This drawback has impeded further improvement of the efficacy of this method, which is crucial for clinical applications. For example, many *in vitro* and *in vivo* studies [14, 28, 44, 45, 47, 59, 61, 68, 93] have been performed to investigate the effect of pulsing parameters, such as pulse number, duration, and polarity, on the efficiency of gene delivery. However, these studies are mostly empirical,

following trial-and-error manners due to the lack of available prediction tools of the process. As a result, clear physical understandings are still lacking in explaining many of the observed trends, and it remains to be a difficult task to extract key information from these studies toward advancing the technique. In this thesis, the author aims to develop a basic understanding of the physical process of electroporation-mediated molecular transport, by performing model studies that connect available theoretical predictions with experimental observations. From an engineering point of view, this work is supposed to benefit experimentalists in providing a powerful prediction tool for the design and optimization of electroporation, and equally benefit theorists to improve the models and advance fundamental understandings in the subject.

Depending on the specific goal of researches or applications, drugs, dyes or potentially therapeutic agents such as proteins, oligonucleotides, RNA and DNA [13], can be selected as the target to be delivered into the cytoplasm via electroporation. These target molecules can vary greatly in size. For example, propidium iodide (PI), a small dye molecule with a molecular mass of 668.4 Da, is frequently used to detect the occurrence of membrane permeabilization [14, 21, 98], while in DNA electrotransfer the molecular mass of delivered polymer chains can easily exceed a million Dalton (corresponding to a chain length of around 1.5 kbp) [21, 22, 32, 81, 98]. Experimental observations suggest that, between these two cases how the target molecules enter the cell can be quite different. Small molecules are more likely to be directly driven across the permeabilized membrane by electrophoresis and diffusion. On the other hand, the transfer of macromolecules such as DNA is presumably more complex [12, 15, 22, 62, 67], and different theories have been presented to hypothesize the mechanisms involved [43, 60, 69, 99, 105]. Consequently, necessity arises to develop different models to capture the key characteristics for each case.

In this thesis, the author implemented models to study the transport of three different types of target molecules: propidium iodide (Chapter 2), Dextran (Chapter 3) and linear double-strand DNA polymer chain (Chapter 4). These molecules are among

the most commonly used targets in electroporation studies, either in research or practical applications. More importantly, they cover three typical sizes of electroporation-mediated delivered agents in hydrodynamic radius: PI, small ( $\sim 0.5$  nm); Dextran of 10k Dalton, moderate ( $\sim 2$  nm); DNA, large ( $>100$  nm). These studies altogether advance the understanding of the various characteristics of electroporation-mediated delivery with respect to the target molecule size. A brief summary of each task is presented below.

- The author implemented a whole-field numerical model to extensively investigate PI transport via electroporation. Furthermore, the results are directly compared with experimental data by Sadik *et al.* [72], which studied PI delivery under a variety of extra-cellular conductivity configurations. The comparison confirms that electrophoretic transport is the dominating mechanism in mediating PI delivery, and the inverse correlation observed between PI delivery and extra-cellular conductivity results from an electrokinetic phenomenon termed Field Amplified Sample Stacking (FASS). The main contribution of this quantitative study lies in providing a more comprehensive mechanistic interpretation to the dynamics of electroporation-mediated molecular delivery. This work is presented in Chapter 2, and has been summarized in a manuscript submitted to *Bioelectrochemistry* [100].
- With the prediction tool used in the previous task, the author examined two-pulse electroporation as a potential means to achieve effective delivery efficiency. In this study, a combination of a strong, short pulse (HV) and a weak, long pulse (LV) is applied. The respective effects of HV and LV are theoretically predicted, and the total delivery of Fluorescein-Dextran is quantitatively correlated with pulsing parameters. Through comparison with experiments by Sadik *et al.* [73], a pore dynamics analysis is presented to explain the existence of a threshold strength of LV, above which the delivery becomes much more effective. This study bears significance in providing theoretical foundation for protocol optimization and useful predictions to guide future experimental studies. This work is presented

in Chapter 3, and has been published in *Biophysical Journal* [73].

- To study DNA electrotransfer, the author developed a theoretical framework to characterize the process of DNA translocation through an electropore with finite pulses. This model study adopts the "translocation theory", which assumes that as a polymer chain DNA molecule can be driven across a narrow electropore like a thread being pulled across a needle hole. Numerical studies were performed to quantitatively investigate the probability of successful DNA translocation across the pore as a function of pulsing parameters. The results are compared with previous experiments and provide theoretical explanations to the trends that was poorly understood previously. A main contribution of this work is to establish a power-law correlation between DNA delivery efficiency and pulsing parameters, which can be verified by well-designed experiments. This work is presented in Chapter 4, and has been published in *BBA Biomembranes* [101].

During the PhD study, the author also began to develop a theoretical model to predict the deformation and relaxation of vesicles and cells suspended in solution. This work follows our previous model studies [103, 104], and aims at quantitatively extracting important mechanical properties of the lipid membrane from temporal-resolved measurements of shape changes. This work is presented in Chapter 5, and is currently under preparation for a journal publication.

Concluding remarks are made in Chapter 6.



## Chapter 2

### Propidium iodide delivery with millisecond electric pulses

#### 2.1 Introduction

As a widely-used technique to deliver active agents into biological cells and tissue [1, 8, 89, 13, 19, 46, 56, 74, 86], the process of electroporation includes two basic aspects. In the first, the application of an electric pulse permeabilizes the membrane to gain access to the cytoplasm [3, 6, 10, 34, 37, 38, 40, 52, 54, 79, 85, 95, 96, 97]. In the second, molecules are transported into the cell via mechanisms such as electrophoresis, diffusion, and endocytosis [1, 14, 28, 43, 44, 45, 47, 59, 63, 61, 64, 68, 69, 93, 94, 78, 81, 90, 99, 105]. In an earlier work by Sadik *et al.* ([72], henceforth denoted as Sadik13), time- and space-resolved fluorescence microscopy was used to quantify the second aspect, namely, the transport of small molecules via electroporation. As a companion study of Sadik13, this model investigation aims to differentiate contributions to total delivery by the various pertinent mechanisms. In addition, it also provides quantitative data to help interpret trends observed in earlier experiments, namely, the inverse correlation between delivery and extra-cellular conductivity [10, 49].

The model used in this chapter couples the asymptotic Smoluchowski equation (ASE) [35, 54, 55] for membrane permeabilization with the Nernst-Planck equations for ionic transport [41, 42]. (A list of abbreviations used in the following chapters is given in Table 2.1.) Following Sadik13, the delivery of propidium iodide (PI) into 3T3 mouse fibroblast cells is simulated. The extra-cellular conductivity is varied between 100 and 2000  $\mu\text{S}/\text{cm}$ . The simulation provides detailed, dynamic predictions that were not directly measured by the experiments, including the systematic behavior of the transmembrane potential (TMP), the membrane conductance, and the pore area density (PAD). On the other hand, the results on PI delivery are compared directly with

Abbreviation	Definition
ASE	asymptotic Smoluchowski equation
FASS	Field-Amplified Sample Stacking
PAD	pore area density
PI	propidium iodide
Sadik13	reference [72]
TFI	total fluorescence intensity
TMP	transmembrane potential

Table 2.1: Definition of abbreviations.

data from Sadik13. This comparison not only validates the numerical model, but also helps tackle the basic physical processes involved in electroporation-mediated molecular delivery. The main contribution of this work lies in providing a clear, thorough physical explanation of the key experimental observation with available theoretical tools. This work has been summarized in a manuscript submitted to *Bioelectrochemistry* [100].

## 2.2 Model formulation

A schematic of the problem is presented in Fig. 2.1. The cell is modeled as a spherical space surrounded by a thin and rigid cell membrane. A constant pulse with the strength of  $E_0$  is applied, and axisymmetry is assumed with respect to the direction of the electric field. A spherical coordinate system  $(r, \theta)$  is adopted, and the cell radius is  $a$ . The axis of symmetry is denoted by  $x$ , which is also the coordinate along the cell centerline. The intra- and extra-cellular conductivities are denoted by  $\sigma_i$  and  $\sigma_e$ , respectively. The PI molecule is a charged ion with a valence number of +2.

The model framework follows that presented in an earlier work by our group [42]. A detailed description of the model is presented in Appendix A. Briefly speaking, the Ohmic equations are solved for the intra-cellular electric potential,  $\Phi_i$ , and the extra-cellular electric potential,  $\Phi_e$ . On the membrane, the current continuity condition is applied:

$$-\mathbf{n} \cdot \sigma_i \nabla \Phi_i = -\mathbf{n} \cdot \sigma_e \nabla \Phi_e = C_m \frac{\partial V_m}{\partial t} + j_p, \quad (2.1)$$

where  $\mathbf{n}$  is the local unit vector normal to the membrane,  $C_m$  is the membrane capacitance, and  $j_p$  is the local ionic current density across electropores. The TMP (denoted by  $V_m$ ) is the potential difference across the infinitesimally-thin membrane. Equation (2.1) is coupled with the ASE for membrane permeabilization to track the evolution of both the electric potential and pore statistics. Once the latter is obtained, the PAD (denoted by  $\rho_p$ ) can be evaluated:

$$\rho_p(t, \theta) = A_p(t, \theta) / \Delta A, \quad (2.2)$$

where  $\Delta A$  is a local area element [35], and  $A_p$  is the total area occupied by the pores thereon. The PAD therefore represents a quantification of the degree of membrane permeabilization. The membrane conductance,  $g_m$ , is calculated by taking the ratio of the local ionic current density and the TMP:

$$g_m(t, \theta) = j_p / V_m. \quad (2.3)$$

To track the evolution of PI concentration, the Nernst-Planck equations are solved in conjunction with the following reactive kinetics:



Here  $\text{PI}^{2+}$  denotes the free PI ion, B denotes the binding sites in the cytoplasm, and PIB is the compound which is responsible for the experimentally observed fluorescence emission.  $k_+$  and  $k_-$  are the association and dissociation constants, respectively. The species concentrations are denoted by  $[\text{PI}^{2+}]$ ,  $[\text{B}]$ , and  $[\text{PIB}]$ , respectively.

A complete description of the model, including the numerical implementation, as well as the boundary and initial conditions, are found in Appendix A. Model parameters specific to the current problem are listed in Table. 2.2, which follows the experimental conditions in Sadik13. Note that in particular a value of 0.16 V was adopted for  $V_{ep}$ , the characteristic voltage of electroporation. The value defers from that used in previous work [35, 41, 42], and is determined from a comparison between experimental data and

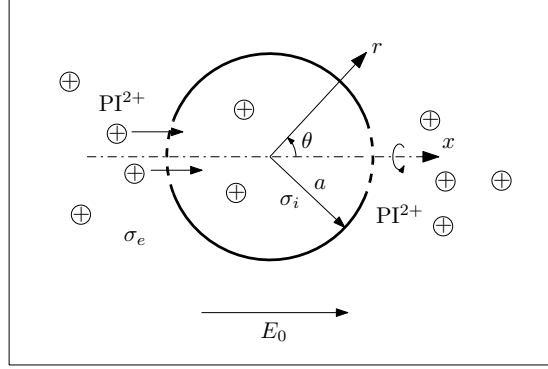


Figure 2.1: A schematic of the problem.  $(r, \theta)$  denotes the spherical coordinate system.  $x$  is the axis of rotation, and is aligned with the direction of field application. The field strength is denoted by  $E_0$ . The intra- and extra-cellular conductivities are denoted by  $\sigma_i$  and  $\sigma_e$ , respectively.

Symbol	Definition	Value/Source
$E_0$	applied field strength	0.8 kV/cm [72]
$t_p$	pulse length	100 ms [72]
$a$	cell radius	7 $\mu\text{m}$ [72]
$\sigma_e$	extra-cellular conductivity	100-2000 $\mu\text{S/cm}$ [72]
$\sigma_i$	intra-cellular conductivity	4000 $\mu\text{S/cm}$ [42]
$[\text{PI}^{2+}]_{e,o}$	initial extra-cellular concentration of $\text{PI}^{2+}$	100 $\mu\text{M}$ [72]
$[\text{B}]_{i,o}$	initial intra-cellular concentration of B	6.93 mM [42]
$V_{ep}$	characteristic electroporation voltage	0.16 V [72]

Table 2.2: List of model parameters in Chapter 2.

model simulation in our recent study [73].

## 2.3 Results

In the following, simulated results are first presented on the effect of extra-cellular conductivity on membrane permeabilization. The results on PI delivery are then presented and compared with experimental data from Sadik13. For all cases, a single pulse of 0.8 kV/cm and 100 ms is applied.

Figure 2.2 summarizes the results on the TMP,  $V_m$ , membrane conductance,  $g_m$ , and the PAD,  $\rho_p$ . Figure 2.2a shows the evolution of  $V_m$  at  $\theta = \pi$  as a function of time. The differences between the cases are only visible in the initial stage ( $\sim 10 \mu\text{s}$ , see the inset), which is caused by the dependence of charging time on the extra-cellular conductivity

[71, 92]. For  $t > 10 \mu\text{s}$ ,  $V_m$  settles to an equilibrium value, which is maintained until the end of the pulse. Figure 2.2b shows  $V_m$  as a function of the polar angle,  $\theta$ , at  $t = 95 \text{ ms}$ . The consistency of the equilibrium distribution with respect to the extra-cellular conductivity is evident. It is found that this equilibrium value of  $V_m$  in the permeabilized regions is determined by a critical point of the pitchfork bifurcation in the  $(r_{eq}, V_m)$  space, where  $r_{eq}$  is the equilibrium pore size at a given voltage. In other words, it is determined by the energy landscape of the porated membrane, which does not change with respect to the extra-cellular conductivity. A more detailed analysis is presented in Section 2.4.

Figure 2.2c shows the evolution of  $g_m$  as a function of time. Similar to  $V_m$ , it exhibits an initial stage of rapid growth, followed by a plateau (an equilibrium) in the presence of the pulse, and a rapid decay post-pulsation. However, the equilibrium value depends strongly and positively on  $\sigma_e$ . This trend is more obviously observed in Fig. 2d, where  $g_m$  at  $\theta = 0, \pi$  and  $t = 95 \text{ ms}$  is plotted against  $\sigma_e$ . This correlation derives from the global Ohmic current balance. In fact, following an analysis similar to that presented in [42], it can be shown that

$$g_m \propto \frac{\sigma_e}{2\sigma_e + \sigma_i} \left( 3 - \frac{2}{E_0 a} \max(|V_m|) \right). \quad (2.5)$$

In Fig. 2.2d, the dashed line represents a fitting in the form  $C\sigma_e/(2\sigma_e + \sigma_i)$ , where the fitting constant  $C = 1.46 \times 10^5 \text{ S/m}^2$ . This result is in qualitative agreement with the numerical study by Suzuki *et al.* [84].

Figures 2.2e and f show the behavior of  $\rho_p$  with respect to time and  $\sigma_e$ . Not surprisingly, the trend concurs with that of  $g_m$ , as the change in the latter is only caused by a change in membrane permeabilization. Note that this result qualitatively defers from that in supra-electroporation, where our model did not indicate a strong dependence of  $\rho_p$  on  $\sigma_e$  [42]. However, in neither situation does membrane permeabilization provide a viable explanation for the negative correlation between delivery and extra-cellular conductivity [10, 49, 72], and alternative mechanisms need to be identified.

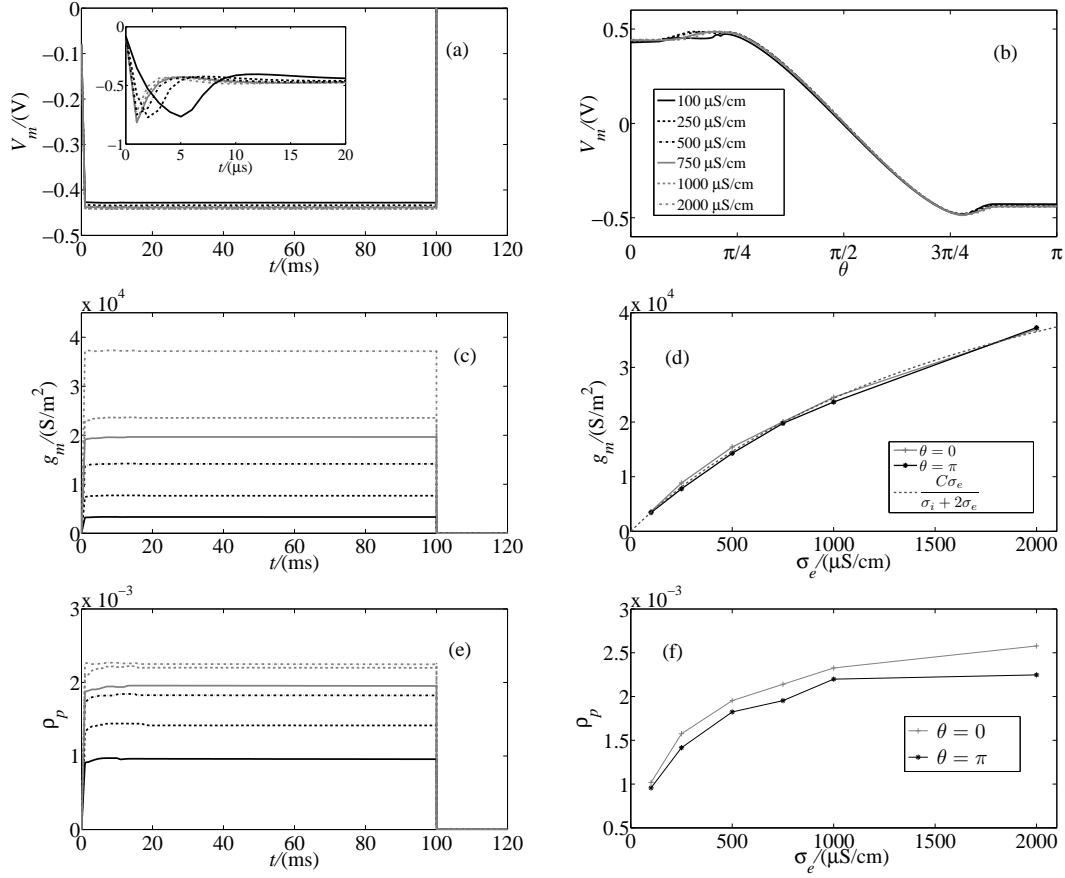


Figure 2.2: Simulated membrane permeabilization under a single pulse of 0.8 kV/cm in strength and 100 ms in length, for various extra-cellular conductivities. (a) Evolution of the TMP,  $V_m$ , at  $\theta = \pi$  as a function of time. (b) Polar distribution of the TMP at  $t = 95$  ms. (c) Evolution of local membrane conductance,  $g_m$ , at  $\theta = \pi$  as a function of time. (d) Membrane conductance at  $\theta = 0, \pi$  at  $t = 95$  ms. The dashed is a theoretical prediction, and the fitting constant  $C = 1.46 \times 10^5 \text{ S}/\text{m}^2$ . (e) Evolution of the PAD,  $\rho_p$ , at  $\theta = \pi$  as a function of time. (f) The PAD at  $\theta = 0, \pi$  at  $t = 95$  ms.

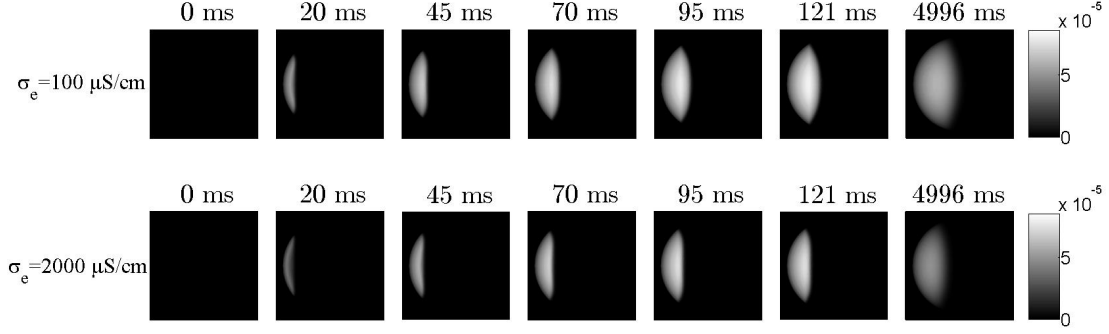


Figure 2.3: Contour plots of convoluted PI concentration at the cell center-plane for  $\sigma_e = 100 \mu\text{S}/\text{cm}$  (top) and  $2000 \mu\text{S}/\text{cm}$  (bottom). The snapshots are taken at  $t = 0, 20, 45, 70, 95, 121$ , and  $4996$  ms, following the experimental presentation in Sadik13.

Figure 2.3 shows exemplary simulated results in an attempt to reproduce the experimental fluorescence images in Sadik13 (Fig. 1 therein). The contour plot is based on the convoluted concentration of PIB:

$$[\text{PIB}]_{\text{conv}} = \int_{-\sigma_z/2}^{\sigma_z/2} [\text{PIB}] e^{-z^2/2\sigma_z^2} dz, \quad (2.6)$$

where  $\sigma_z$  is the focal depth of the microscopic system, and  $z$  is the axis perpendicular to image acquisition. This convolution is taken to approximate the effects of a finite focal depth in the experimental measurements [41]. The evolution with respect to the lowest ( $100 \mu\text{S}/\text{cm}$ ) and the highest ( $2000 \mu\text{S}/\text{cm}$ ) conductivities is shown, which is in qualitative agreement with data. Noticeably, the spread is stronger in case of  $\sigma_e = 100 \mu\text{S}/\text{cm}$ .

Figure 2.4 demonstrates the detailed evolution of the species concentrations, also for the two extreme values of  $\sigma_e$ . Figures 2.4a-d show  $[\text{PI}^{2+}]$  and  $[\text{B}]$  at different times along the cell centerline,  $x$ . Together, the results indicate that the binding sites are exhausted upon electrophoretic entry of the free ions in the presence of the 100-ms pulse. Continuous intra-cellular diffusion and association/dissociation occur after the pulse ceases. However, no appreciable molecular exchange across the membrane is predicted. Figures 2.4e and f show the  $[\text{PIB}]$  profile. This compound is responsible for the experimentally observed fluorescence emission, and the convoluted concentration as defined by Eq. (2.6) is assumed to be proportional to the fluorescence intensity. During

the pulse, the front of [PIB] profile advances uniformly along the field direction due to binding-site exhaustion. The redistribution post-pulsation is due to intra-cellular redistribution of all species. In comparison with Fig. 2.3, the peaks observed therein are attributed to the convolution over a spherical cell geometry, which effect has been explained in a previous work of our group [41]. Finally, Figs. 2.4g and h show the sum of the free and bound ions. This quantity indicates the total PI concentration in the cell. For both values of  $\sigma_e$ , this summed concentration ( $\sim 10$  mM) is significantly higher than the extra-cellular PI concentration ( $100 \mu\text{M}$ ). Furthermore, consistent with the experimental observation, delivery decreases when  $\sigma_e$  increases. These trends are explained with an electrokinetic phenomenon termed Field-Amplified Sample Stacking (FASS), which is discussed in greater details in our previous work [41, 42].

To study total delivery, the free and bound PI concentrations are respectively integrated over the entire cell and then summed, and the resulting quantity is denoted by  $\text{PI}_{\text{tot}} + \text{PIB}_{\text{tot}}$ . The evolution of total delivery as a function of time and for the six values of  $\sigma_e$  is shown in Figs. 2.5a and b, where Fig. 2.5b displays the specific stage during the pulse. Once the pulse ceases, the total delivery,  $\text{PI}_{\text{tot}} + \text{PIB}_{\text{tot}}$ , does not further increase. This saturation of delivery is due to the fact that in the model, pores immediately return to a very small size ( $r_m = 0.8$  nm, [35]), hence significantly diminishing  $\rho_p$  and preventing post-pulsation diffusive delivery. A further examination on the effect of the latter is presented later in Fig. 2.6b. Figures 2.5c and d show the evolution of bound PI integrated over the whole cell ( $\text{PIB}_{\text{tot}}$ ). The results are in qualitative agreement with the total fluorescence intensity (TFI, induced by the compound PIB) presented in Sadik13. Figure 2.5c shows, in contrast to Fig. 2.5a, that  $\text{PIB}_{\text{tot}}$  continues to increase even after the pulse ceases. Although no more PI is delivered into the cell at this stage, the available free PI ions that have already entered the cell during the pulse (Figs. 2.4a and b) continue to spread and bind, causing  $\text{PIB}_{\text{tot}}$  to further increase. A final steady-state is reached within the diffusive time scale ( $\sim 0.1$  s) after the association/dissociation processes equilibrate over the entire cell.

Together, Figs. 2.4 and 2.5 impart important insights. First, due to the FASS



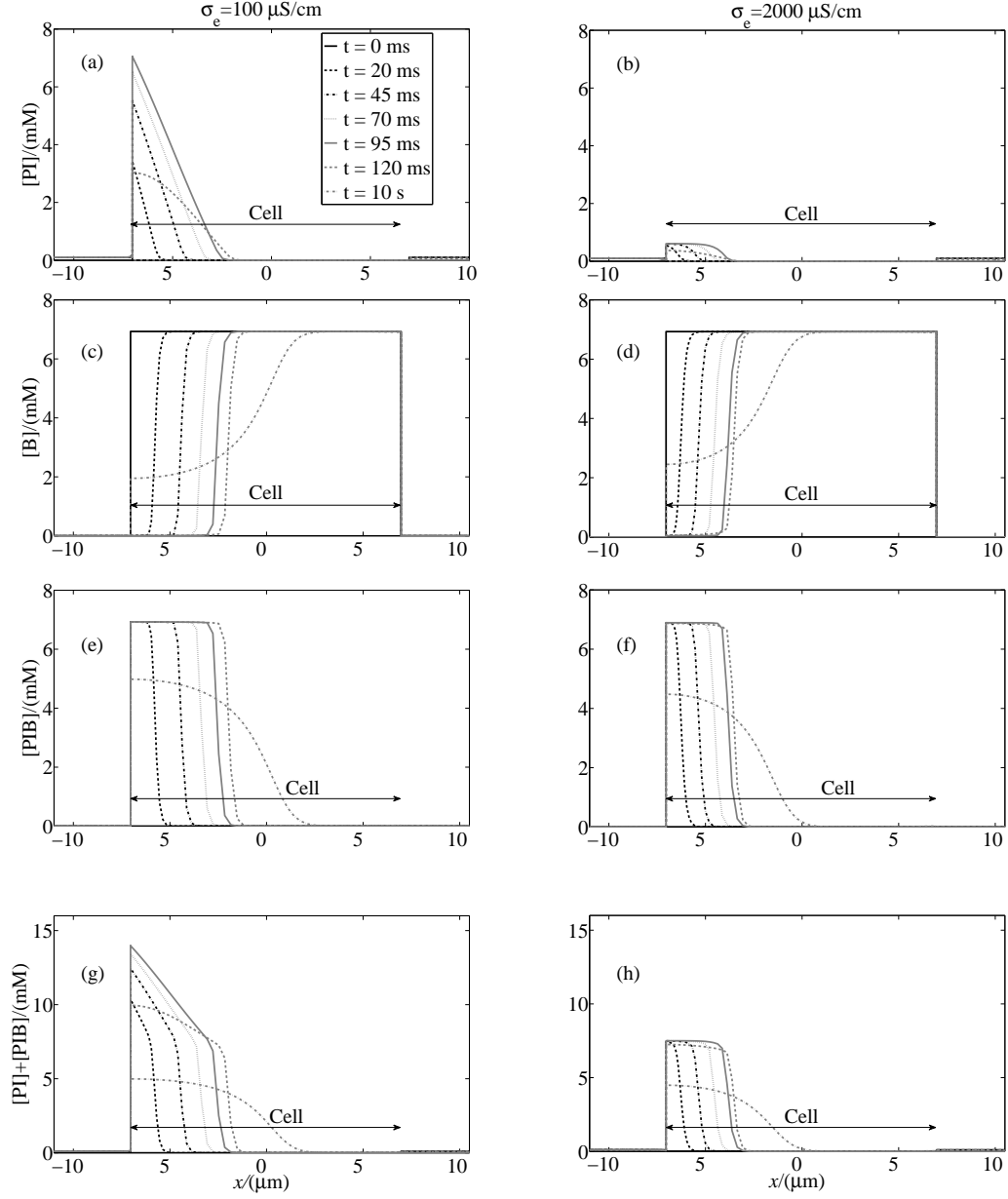


Figure 2.4: Species concentration evolution for  $\sigma_e = 100 \mu\text{S}/\text{cm}$  and  $2000 \mu\text{S}/\text{cm}$  along the cell centerline,  $x$ .

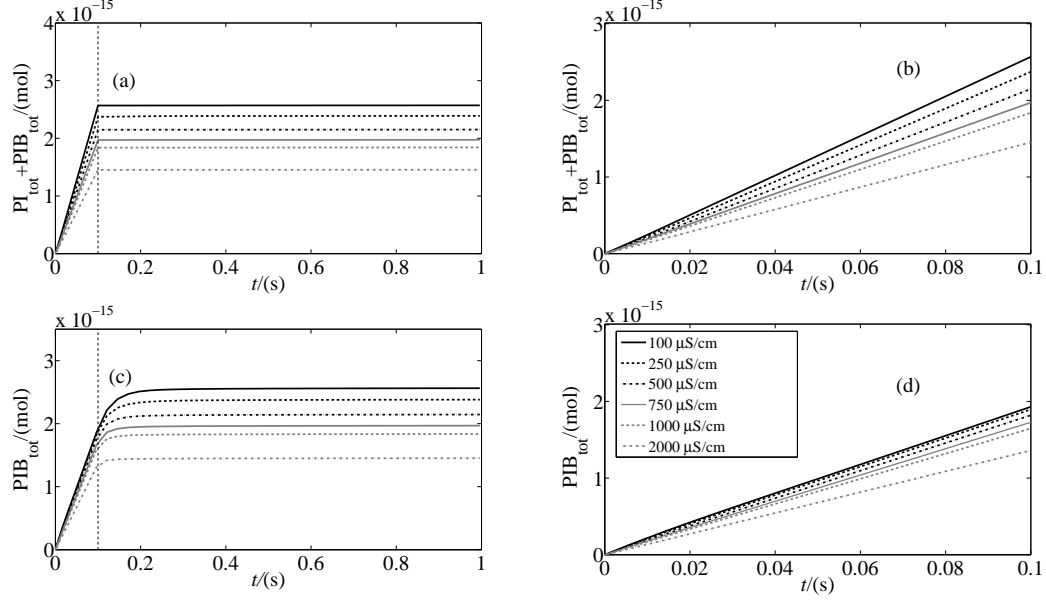


Figure 2.5: (a) Evolution of integrated free PI and PIB concentrations over the entire cell ( $PI_{tot} + PIB_{tot}$ ) for the six values of  $\sigma_e$ . The dashed vertical line indicates the end of the pulse. (b) Evolution of  $PI_{tot} + PIB_{tot}$  during the pulse. (c) Evolution of integrated PIB concentration over the entire cell ( $PIB_{tot}$ ). (d) Evolution of  $PIB_{tot}$  during the pulse.

mechanism and the high conductivity ratio, the cell can be “loaded” with a high concentration of ions via electrophoretic transport, even with short pulses. In the current simulations, this “loading” is sufficient to exhaust locally the high concentration of binding sites. A similar conclusion can be drawn if PI is replaced by other target agents such as drug molecules. Second, the observed increase in fluorescence signal post-pulsation, such as that presented in Sadik13 may be partially attributed to this “pre-loading” effect. Therefore, caution needs to be taken to interpret experimental data where an indirect indicator such as PIB is used to study PI delivery.

Figure 2.6a compares the simulated results with data from Sadik13. The experimental data is denoted by circles, and the middle and lower curves represent contributions to the normalized TFI during and after the pulse, respectively. The upper curve is the sum of the two. The model prediction is denoted by pluses, and the definition of the curves follows the data. Because of the difference in the units of the measurement (a.u. for the fluorescence signal) and the prediction (mol for  $PIB_{tot}$ ), the axis presenting the latter is scaled linearly, such that the upper curves are best matched. The comparison

demonstrates that the trends in the data are very-well captured by the numerical study, although quantitative differences are observed between the middle and lower curves. As noted above, in the model prediction, although  $\text{PIB}_{\text{tot}}$  continues to increase after the pulse, it is in actuality attributed to further binding of the free PI ions already delivered into the cell during the pulse.

The correlation between  $\text{PIB}_{\text{tot}}$  and  $\sigma_e$  can be approximated by

$$\text{PIB}_{\text{tot}} \propto \frac{1}{2\sigma_e + \sigma_i}. \quad (2.7)$$

A fitting using this functional form is shown as the dotted line in Fig. 2.6a. This correlation can be derived if it is assumed that delivery is primarily mediated by electrophoresis. The molar flux into the cell is proportional to  $c_e E_e$ , where  $c_e$  is the extra-cellular concentration of  $\text{PI}^{2+}$ , and is assumed to be constant ( $[\text{PI}^{2+}]_{e,o}$ ). Therefore, molecular delivery is proportional to the extra-cellular field strength at the membrane. Using Eq. (2.1), the steady-state expression of  $E_e$  is given by

$$E_e = \frac{g_m V_m}{\sigma_e}. \quad (2.8)$$

Substituting Eq. (2.5) into Eq. (2.8), and considering  $V_m$  does not change with respect to the extra-cellular conductivity, the correlation (2.7) is obtained.

In the simulation above, and similar to our previous studies [41, 42],  $\rho_p$  decreases by three orders of magnitude immediately after the pulse ceases, due to the shrinking of the pore size in the absence of  $V_m$ . This reduction prohibits appreciable diffusive transport afterwards. This behavior is an artifact of the ASE model due to its incapability to include the resealing process (typically on the order of seconds to minutes [13, 25, 95]). To investigate the effects of post-pulsation diffusion,  $\rho_p$  reduction at the end of the pulse is artificially prevented in the simulations. In other words,  $\rho_p$  is kept at its value at the end of the pulse for an additional second. The result is shown in Fig. 2.6b, also in comparison with the data. Similarly, the axis for  $\text{PIB}_{\text{tot}}$  is rescaled to best match the upper curves. It is observed that the respective contributions from during and after the pulse match better quantitatively when compared with Fig. 2.6a. However, the inverse

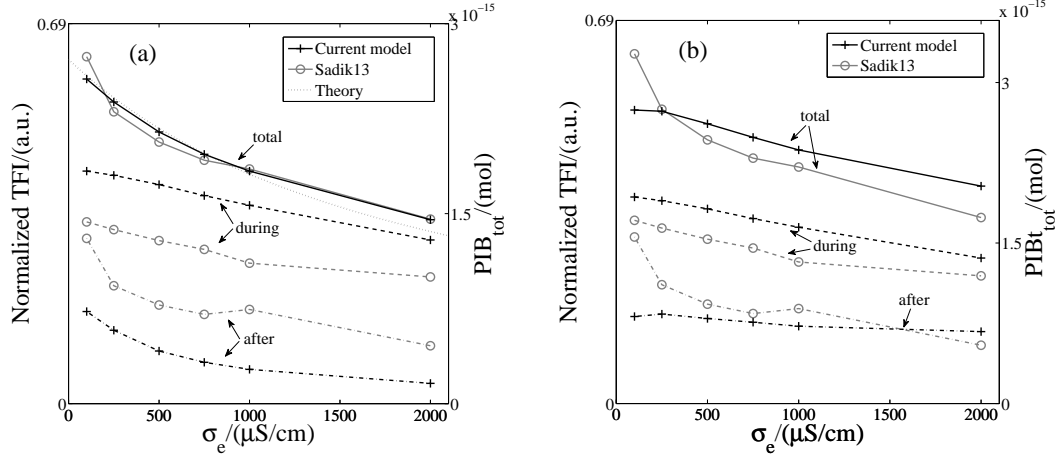


Figure 2.6: Comparison of simulated results ('+', right axis) with experimental data from Sadik13 ('o', left axis). For the data, the middle and lower curves represent contributions to the total fluorescence intensity (TFI) during and after the pulse, respectively. The upper curve is the sum of the two. In comparison, numerical simulation of  $\text{PIB}_{\text{tot}}$  is presented, and the upper, middle, and lower curves are defined similarly. The right axis is scaled linearly such that the upper curves from data and simulation best match. (a) Simulated results using the original ASE model. The dotted line is a theoretical fitting with the functional form  $C/(2\sigma_e + \sigma_i)$ . (b) The size of the pores are artificially maintained for 1 s post-pulsation in the ASE model to allow for more diffusive delivery.

trend with respect to  $\sigma_e$  is abated. This result is not surprising, as diffusive transport correlates positively with  $\rho_p$ , which in turn depends positively on  $\sigma_e$  (Fig. 2.2f). The addition of the diffusive delivery therefore weakens the inverse trend observed in the data.

In summary, the model prediction agrees qualitatively with the experimental data in general, and quantitatively in terms of the correlation between delivery and the extracellular conductivity (Eq. (2.7)). The results confirm that this inverse correlation is primarily mediated by electrophoretic transport during the pulse. In fact, this trend tends to be abated rather than enhanced by diffusive transport due to the positive dependence of permeabilization on extra-cellular conductivity. The current study suggests that electrophoretic transport may be important even for a small molecule such as PI.

## 2.4 The equilibrium transmembrane potential

In Fig. 2.2b, it is found that the TMP,  $V_m$ , settles to an equilibrium value in the permeabilized regions within a few microseconds after the pulse starts. Furthermore, this value does not vary appreciably with respect to the extra-cellular conductivity. Here this value is argued to be determined by a critical point in the pitchfork bifurcation in the  $(r_{eq}, V_m)$  relation, where  $r_{eq}$  is the equilibrium pore size at a given voltage.

In the ASE used, and in general in the Smoluchowski equations governing the pore dynamics [17, 35, 54], the pore size evolves to minimize membrane energy. The rate of change is given by the equation [35]:

$$\dot{r} = \frac{D}{K_B T} \left[ \frac{4r_p^4 \beta}{r^5} - 2\pi\gamma + 2\pi\sigma_{eff}r + \frac{F_{max}V_m^2}{1 + \frac{r_h}{r+r_t}} \right], \quad (2.9)$$

where  $r$  is the pore radius,  $D$  is the pore radius diffusion coefficient,  $K_B$  is the Boltzmann constant, and  $T$  is temperature. The value of  $\sigma_{eff}$  is given by  $\sigma_{eff} = 2\sigma' - \frac{2\sigma' - \sigma_0}{(1 - \rho_p)^2}$ .  $\beta$ ,  $\gamma$ ,  $F_{max}$ ,  $r_h$ ,  $r_c$ ,  $\sigma'$ , and  $\sigma_0$  are model constants, and the values can be found in [35]. This equation can be written in a generalized form as:

$$\dot{r} = U(r, V_m, \rho_p). \quad (2.10)$$

The equilibrium value for the pore size,  $r_{eq}$ , can be found by setting the right hand side of Eq. (2.10) to zero:

$$U(r_{eq}, V_m, \rho_p) = 0. \quad (2.11)$$

In general, the dependence of  $r_{eq}$  on  $\rho_p$  is weak. On the other hand, its dependence on  $V_m$  exhibits an interesting pitchfork bifurcation, which is shown in Fig. 2.7a, for an exemplary value of  $\rho_p = 2 \times 10^{-3}$ .

The coupled dynamics between  $r_{eq}$  and  $V_m$  in the initial charging and permeabilization processes are illustrated in Figs. 2.7a and b, where the four stages are denoted by I-IV. In Stage I, the initial charging stage, the membrane is near-impermeable with sub-nanometer pores, and  $V_m$  grows rapidly via capacitive charging (see Eq. (2.1)). Once  $V_m$  reaches  $V_m^{crit}$ , the bifurcation point, pores begin to expand significantly. Due

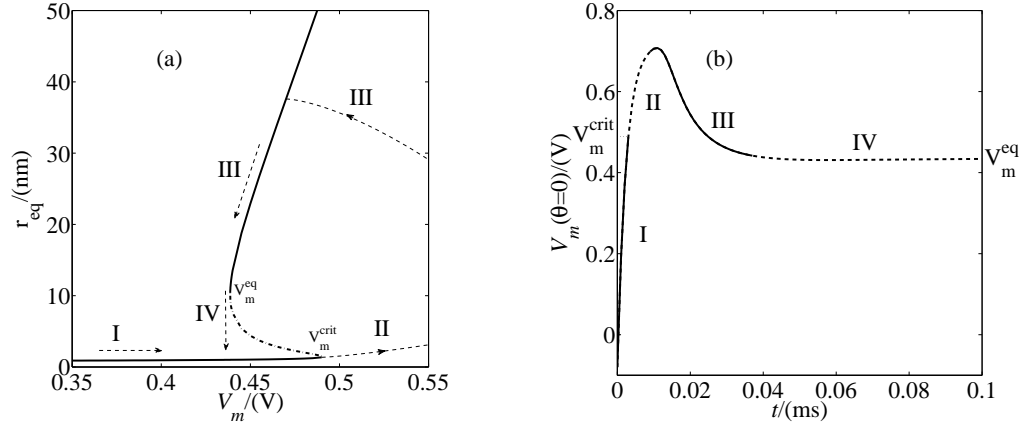


Figure 2.7: Schematics for the  $(r_{eq}, V_m)$  dynamics. (a) The relation between  $r_{eq}$  and  $V_m$  exhibits a pitchfork bifurcation behavior. Between  $V_m^{eq}$  and  $V_m^{crit}$ , three branches of solutions exist from Eq. (2.11), where the middle one (dash-dotted) is unstable. The initial charging and permeabilization process follows four stages denoted by I-IV. For this case  $\rho_p = 2 \times 10^{-3}$ . A detailed description is given in the text. (b) Exemplary evolution of  $V_m$  as a function of time. The stages I-IV correspond to those in (a).

to the consequent “jump” in  $g_m$  (Stage II),  $V_m$  eventually has to decrease to satisfy the current continuity condition (Stage III), until the upper branch of the bifurcation is reached.  $V_m$  continues to decrease until it reaches the other critical point,  $V_m^{eq}$ , where the pore size begins to recover to the lower branch (Stage IV). The dependence of pore radius on  $V_m$  exhibits hysteresis typical of this type of bifurcation. The point around  $V_m^{eq}$  is the most interesting, because two equilibrium pore sizes exist. For this reason,  $g_m$  can assume a range of values for a single value of  $V_m$ . The upper bound can be calculated by assuming all pores are on the upper branch,  $r_{eq} = 10.4$  nm; the lower bound, the lower branch,  $r_{eq} = 1.01$  nm. If the required steady-state value of  $g_m$  to satisfy the current continuity condition (Eq. (2.1)) lies within these two bounds, then  $V_m$  maintains at the level of  $V_m^{eq}$ . This phenomenon is analogous to phase change in physics, where  $V_m^{eq}$  assumes the role of, e.g., temperature. For the same argument,  $V_m^{crit}$  is another candidate for the equilibrium value of  $V_m$ , which in general occurs when less number of pores are locally available, e.g., at the edges of the permeabilized regions. (See the slightly increased  $V_m$  values near  $\theta = \pi/4, 3\pi/4$  in Fig. 2.2b.) Although the above illustration is only schematic, the full-model simulation follows this general pattern.

As a conclusive remark, this finding bears significance in that it connects the mesoscopic ASE model with macroscopic observables. The membrane energy model in the ASE, based on which Eq. (2.9) is derived, has a few free constants. In general, these constants cannot be directly measured. The above analysis reveals that if pores on the membrane do follow the bifurcation behavior with respect to the TMP, then the critical values, namely,  $V_m^{eq}$  and  $V_m^{crit}$  can be directly observed via a fluorescence measurement similar to that by Kinoshita *et al.* [31] or Flickinger *et al.* [16]. These values can in turn help determine the pertinent constants (such as  $\beta$ ,  $\gamma$ , and  $F_{max}$ ) used in the model.

## 2.5 Conclusions

In this work, a companion model study is implemented for the experimental counterpart by Sadik *et al.* [72]. Results on both membrane permeabilization and molecular delivery are presented, through which useful insights on the system behavior are gathered.

The TMP in the permeabilized regions exhibits a consistent value across all six extra-cellular conductivities examined. Through a detailed investigation, it is found that this value corresponds to a bifurcation point in the relation between equilibrium pore size and the TMP. This finding bears significance in that it connects the mesoscopic ASE model with macroscopic observables. In other words, this critical value was previously specified empirically in the ASE model; with the current theory, it can be directly measured by fluorescence techniques following Kinoshita *et al.* [31] or Flickinger *et al.* [16].

Both the PAD and the membrane conductance are predicted to increase with an increasing extra-cellular conductivity. These correlations naturally result from the requirement to satisfy the Ohmic current conservation condition. In fact, the relation between membrane conductance and extra-cellular conductivity follows the functional form of  $g_m \propto \sigma_e / (2\sigma_e + \sigma_i)$ , which can be derived from an idealized model for the electric potential. This positive correlation between membrane permeabilization and extra-cellular conductivity rules out pure diffusive transport as a viable interpretation for the opposite effect of the latter on delivery.

For PI delivery, the model correctly predicts the inverse dependence on extra-cellular conductivity. This agreement confirms that this behavior is primarily mediated by electrophoretic transport during the pulse. In fact, diffusion tends to abate rather than enhance the trend. The correlation between delivery and extra-cellular conductivity is quantitatively captured by the model, namely,  $\text{PIB}_{\text{tot}} \propto 1/(2\sigma_e + \sigma_i)$ . The simulation also reveals that an increase in the fluorescence intensity after the pulse ceases is not necessarily attributed to molecules entering the cell during this time; it may rise from continuous spreading and binding of free ions “loaded” into the cell in the presence of the pulse. Together, the results suggest that electrophoretic transport is important even for a small molecule such as PI.

Last but not least, a direct comparison between experimental data and model simulation as presented in this work helps establish confidence in and validate the latter. In the ASE model, a few parameters (such as  $\beta$ ,  $\gamma$ , and  $F_{\text{max}}$ , see Eq. (2.9) in Section 2.4) are specified empirically following previous work. However, membrane permeabilization (including the PAD and membrane conductance) is found not to depend critically on the specific values of these parameters. Instead, the bifurcation point of the TMP, together with the Ohmic current conservation law strongly regulate the permeabilization behavior. The model therefore provides robust predictions which are useful for the study of electroporation-mediated molecular delivery.



## Chapter 3

### Double-pulse electroporation

#### 3.1 Introduction

Despite all the advantages of the technique, a major deficiency of electroporation is the often low delivery efficiency and/or the accompanied high cell deaths. In many cases, longer exposure under electric field(s) or application of stronger pulse(s) leads to higher efficiency and lower viability at the same time [5, 18]. In other words, delivery and cell viability appears to correlate with each other inversely. Such characteristics hence make tuning of pulsing parameters (shape, strength, duration etc.) a key step toward optimized protocols [5, 14, 33, 63, 68]. Among the efforts that have been made to overcome this difficulty, combination of a strong, short pulse (HV) followed by one or several weak, long pulses (LV) has become a popular approach among researchers. Here the basic idea is to treat permeabilization and transport as separate tasks, which are accomplished by HV (mediating permeabilization) and LV(s) (mediating transport), respectively. The application of HV is a necessary condition to permeabilize the cell membrane, which requires a relatively high field strength to overcome the threshold of the TMP. Once permeabilization is achieved, LV(s) of a lower field strength is applied to decrease cell damage to an acceptable level while still mediating considerable delivery. This approach has been proven to be more effective than single-pulse electroporation by many studies [1, 2, 4, 28, 94, 81]. However, there still lacks any systematic investigation to characterize the scaling behavior between inputs (pulsing parameters) and outputs (delivery efficiency and cell viability) of this technique.

To address this problem in a more systematic way, Sadik *et al.* [73] performed double-pulse electroporation (HV+LV) experiments to quantify the effect of pulsing

parameters on delivery efficiency of Dextran and cell viability. By establishing empirical correlations between inputs and outputs, optimized protocols that maximize the delivery efficiency can be found at any given level of cell viability. In this chapter, the author presents a whole-cell level model study to provide mechanism-based interpretations of the observed experimental trends. More specifically, the total delivery of Dextran is investigated as a function of key pulsing parameters, and the results are directly compared with the experimental data. The main contribution of this work lies in providing theoretical foundation for protocol optimization and useful predictions to guide future experimental studies. This work has been included in a manuscript published in *Biophysical Journal* [73].

### 3.2 Summary of key observations

In Sadik *et al.*'s experiments [73], Fluorescein-Dextran (FD) with a molecular weight of around 10,000 Da were delivered into suspended NIH 3T3 mouse fibroblast cells via electroporation. Note that different from Chapter 2, there is no chemical binding effect involved in this study. A double-pulse protocol was always used, which comprised an HV of 1.0 kV/cm in strength and 1 ms in length and a subsequent LV of various strengths and lengths with no delay. Data of delivery and cell viability were collected by flow cytometry based on a population of 10,000 cells. A detailed description of data analysis approach can be found in [73].

From their experimental study, Sadik *et al.* found that the total delivery of FD increases linearly with the length of LV,  $t_2$  (Fig. 3.1a). The delivery rate per unit time  $\tau_f$  is a function of the strength of LV,  $E_2$ , which appears to be in a sigmoidal-like shape, as shown in Fig. 3.1b. On the other hand, the cell viability  $S$  (%) was found to approximately correlate with the electrical energy of LV  $E_2^2 t_2$  linearly with a negative slope (see Fig. 7 in [73]). These empirical scaling relationships altogether make it possible to identify an optimal value of  $E_2$  at any given level of cell viability, at which the delivery efficiency reaches its maximum. Sadik *et al.*'s experimental work provides a systematic way of pursuing optimization of pulsing parameters, which can possibly be generalized to other cell and target molecular type.

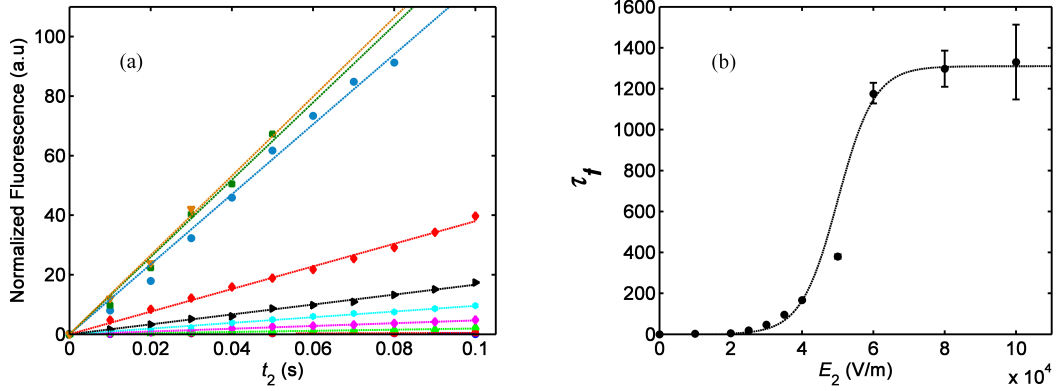


Figure 3.1: Experimental results by Sadik *et al.* [73]. (a) The normalized Fluorescence (NF) of intracellular Fluorescein-Dextran as a function of  $t_2$ . Symbols represent experimental data; curves, least-square fitting corresponding to different cases ( $E_1$  varying between 10,000 and 100,000 V/m from bottom to top). (b) Measured delivery rate per unit time ( $\tau_f$ , circles) as a function of  $E_2$ . The error bars represent the 95% confidence interval of the fitting. The correlation between  $\tau_f$  and  $E_2$  can be further approximated by a least-square sigmoidal fitting (dashed). The coefficient of determination is  $R^2 = 0.97$ .

In Sadik *et al.*'s work, an optimized value of  $E_2$  can be mathematically found within the regime studied because of the following fact: the delivery rate  $\tau_f$  displays a sharp increase when  $E_2$  exceeds a critical field strength of about 25,000 V/m (see Fig. 3.1b). As the cell viability  $S$  decreases linearly to  $E_2^2$ , this abrupt increase in delivery rate with respect to  $E_2$  needs to be locally “sharper” than a quadratic power-law to create a local maximum of delivery at a given value of  $S$ . On the other hand, the underlying mechanism that is responsible for the existence of such a threshold field strength remains to be a mystery. Theoretical studies are therefore necessary to shed light on the physics behind this interesting and important behavior.

### 3.3 Model formulation

The model framework of this chapter follows exactly that in Chapter 2. Model parameters and pulsing schemes are tuned to Sadik *et al.*'s experiments [73], and are listed in Table 3.1.

Symbol	Definition	Value/Source
$E_1$	field strength of HV	1.0 kV/cm
$t_1$	pulse length of HV	1 ms
$E_2$	field strength of LV	0.1-1.0 kV/cm
$t_2$	pulse length of LV	0-100 ms
$a$	average cell radius	7 $\mu\text{m}$
$\sigma_e$	extra-cellular conductivity	100 $\mu\text{S/cm}$
$\sigma_i$	intra-cellular conductivity	4000 $\mu\text{S/cm}$
$[\text{FD}]_{e,o}$	initial extra-cellular concentration of Fluorescein-Dextran	100 $\mu\text{M}$
$V_{ep}$	characteristic electroporation voltage	0.16 V

Table 3.1: List of model parameters in Chapter 3.

### 3.4 Results

Figure 3.2 shows the simulated results of total delivery of Fluorescein-Dextran (TFD) as a function of  $t_2$  for various values of  $E_2$ . It is observed that TFD is always linearly correlated with  $t_2$ , which agrees with the experimental results (Fig. 3.1a). This observation is also consistent with our studies of PI delivery, suggesting that the electrophoretic transport is still the dominating mechanism for a larger target molecule like Dextran.

As the main objective of this investigation, Figure 3.3 shows simulated results of the delivery rate  $\tau_f$  (the left axis) plotted as a function of  $E_2$ . Here  $\tau_f$  is defined as the slopes of fitting lines in Fig. 3.2 corresponding to each value of  $E_2$ . When compared with the experimental trends in Fig. 3.1b, the simulations qualitatively capture a critical value of  $E_2$  above which the delivery rate displays a sharp increase, however at a higher value of 50,000 V/m. This behavior is explained as a result of an abrupt increase of the total permeabilized area (TPA), which is also plotted as a function of  $E_2$  in Fig. 3.3 on the right axis. Here the TPA is defined by the following formula:

$$\text{TPA} = \int_0^{2\pi} d\phi \int_0^{\pi/2} \rho_p d\theta, \quad (3.1)$$

where  $\phi$  is the azimuthal coordinate, and the definition of  $\rho_p$  and  $\theta$  follow those in Chapter 2. Equation (3.1) calculates the total area occupied by electropores on the cathode-facing hemisphere of the cell membrane, which are accessible for the delivery of negatively-charged FD molecules during the pulse. This calculation is performed

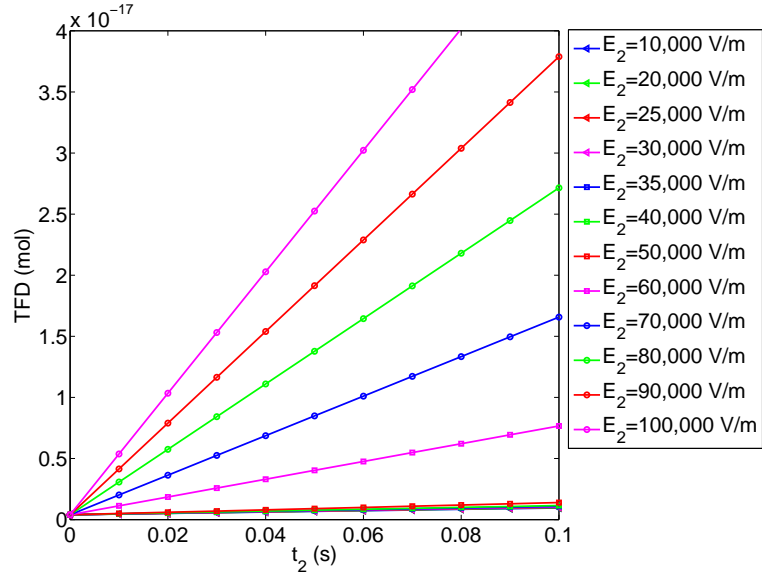


Figure 3.2: Simulated results of total delivery of Fluorescein-Dextran (TFD), plotted as a function of  $t_2$  for  $E_2$  varying between 10,000 and 100,000 V/m.

at  $t = 5$  ms during the second pulse when the permeabilization level has reached its equilibrium. As the TPA and  $\tau_f$  displays very similar trends with respect to  $E_2$ , especially on a sharp “turning point” at about 50,000 V/m, it is intuitive to see that the critical value of  $E_2$  results from a surge in TPA as more open area becomes accessible for FD molecules to enter the cell via electrophoresis.

Through carefully tracking the evolution of pore statistics in the previous simulations, the critical phenomenon of TPA in the simulation is found to be mediated by the same pore dynamics discussed in Section 2.4. In double-pulse electroporation, the TMP of permeabilized region will drop significantly when LV (of a lower strength) replaces HV as the applied field. In the simulation, such a drop of TMP will lead to a decrease in TPA in a short period of time ( $< 100 \mu\text{s}$ ), as shown in Fig. 3.4. According to Fig. 2.7, the decrease in TPA corresponds to “immediate shrink” of large pores (upper branch,  $> 10$  nm in size) to much smaller ones (lower branch,  $\sim 1$  nm in size) at a critical TMP value of  $V_m^{eq}$ , such as to satisfy the current continuity condition. Below a critical value of  $E_2$  (from Fig. 3.4, between 50,000 and 60,000 V/m), the balance has to be established by eliminating all large pores, therefore with only a very small portion

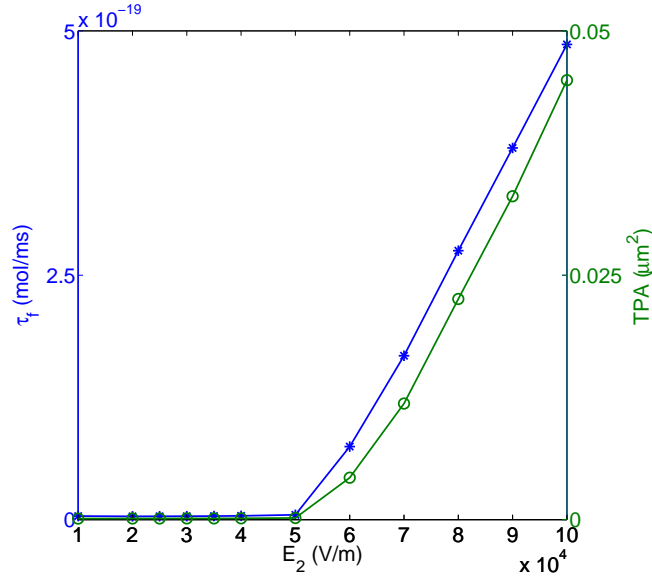


Figure 3.3: Simulated results of delivery rate per unit time  $\tau_f$  (the left axis) and the total permeabilized area (TPA, the right axis) plotted as a function of  $E_2$ .  $\tau_f$  is defined as the slopes of fitting lines in Fig. 3.2 corresponding to each value of  $E_2$ . TPA is defined as the total area occupied by electropores on the cathode-facing hemisphere of the cell membrane.

of open membrane area left compared to that during the first pulse. This bifurcation behavior of equilibrium pore size around  $V_m^{eq}$  is therefore the cause of the existence of a very nonlinear “turning point” of TFD and TPA at a critical value of  $E_2$ .

Although the simulation does not capture the critical value of  $E_2$  quantitatively, here the author argue that the discrepancy is attributed to inaccurate values of model parameters used in the ASE model. In general, a change in the critical value of  $E_2$  is expected when the cell type is changed, which naturally corresponds to a different set of model parameter values. Similar to that in Chapter 2, this study again connects the mesoscopic ASE model with macroscopic observables in the critical value of  $E_2$ . This can be helpful in determining the values of pertinent constants in the ASE model for various cell types.

On the other hand, the simulation also does not capture the plateau in Fig. 3.1b. This behavior is speculated to result from a higher cell death rate at a field strength approaching 100,000 V/m. Briefly speaking, because FD molecules do not bind within

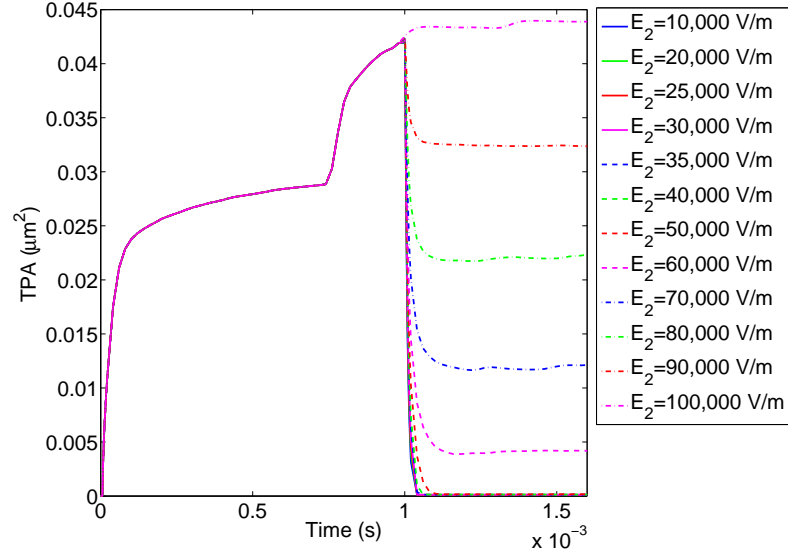


Figure 3.4: Evolution of the TPA during HV (0-1 ms) and at the beginning of LV (1-1.6 ms), with  $E_2$  varying between 10,000 and 100,000 V/m.

the cell, they may eventually diffuse out of the cell if the membrane remains open for an extended period of time, e.g. in case of cell death. The enhanced delivery therefore does not manifest itself in the data. This effect cannot be captured by the transport model, which does not include viability predictions.

### 3.5 Conclusions

In this work, the effect of pulsing protocol on delivery efficiency is investigated with the prediction tool developed in the previous task. This study is a companion research of Sadik *et al.*'s experiments [73], which quantified the Dextran delivery and cell viability using double-pulse electroporation. In the experiments, one of the most important observations is that there exists a threshold value of  $E_2$  above which the delivery efficiency sees a sharp increase. The current study qualitatively captures this trend, and further reveals that this behavior can be attributed to an abrupt shrink in the equilibrium pore size at that critical point. In addition, simulated results confirm that electrophoretic transport is still the dominating mechanisms for a moderate-size target molecule of molecular weight around 10,000 Da.

This study also makes interesting predictions that can be verified by well-designed experiments. First, given the assumption that the critical value of  $E_2$  is caused by the dynamics of membrane permeabilization, then this value should be strongly dependent of cell type. Second, if the critical value of  $E_2$  does correspond to the value of  $V_m^{eq}$  as defined in Section 2.4, then there should exist another critical value of  $E_1$  corresponding to the value of  $V_m^{crit}$ , which is supposed to be the commonly known “critical transmembrane potential”. This value can be captured by investigating the effects of  $E_1$  on the total delivery of FD, and is predicted to be larger than the critical value of  $E_2$  according to Fig. 2.7 ( $V_m^{crit} > V_m^{eq}$ ).

As a summary, this research makes successful connection between the mesoscopic ASE model and experimental observables, hence benefiting both experimentalists and theorists in providing the necessary information they need. In particular, the study provides theoretical foundation for protocol optimization in electroporation, which is useful to guide future studies in the field.



## Chapter 4

### DNA translocation through an electropore

#### 4.1 Introduction

Compared to small molecules, the transfer of macromolecules such as DNA is believed to be more complex. Although many studies [14, 28, 44, 45, 47, 59, 61, 68, 93] have been carried out to optimize the transfection efficiency (TE) of gene transfer, a comprehensive understanding of the process has yet to be established [13]. (A list of abbreviations used in this chapter is given in Table 4.1) One of the key differences between the delivery of DNA and small molecules is that the former stays much longer at the membrane, forming the so-called DNA-membrane complex [12, 15, 22, 62, 67]. The detailed structure of these complexes is still under debate. One theory hypothesizes that the internalization of DNA is facilitated by endocytosis, which is termed the "endocytosis theory" henceforth [43, 69, 99, 105]. In particular, a recent work by Wu *et al.* found that the TE is significantly decreased if certain endocytic mechanisms were inhibited, providing support for this hypothesis [99]. The results are, however, not yet conclusive. For example, a recent experiment by Pavlin *et al.* [60] indicates no significant correlation between the field strength and intracellular vesiculation, which is presumably required for endocytosis.

Meanwhile, other mechanisms for DNA electrotransfer have not been sufficiently explored. In this work, we focus on the so-called "translocation theory". In this theory, macromolecules also go through the membrane like the small ones. However, the process is more complex due to their polymeric nature, and the translocation time can be long, which potentially explains the long coherence time of the DNA-membrane complex [15, 22]. We are motivated by experimental observations from the literature.

In Sukharev *et al.*, the authors observed that the existence of DNA in the buffer solution greatly enhanced cell uptake for smaller molecules such as Dextran [81]. This observation can be explained by prolonged and enlarged pore openings due to DNA molecules “stuck” within the pore. As discussed in Chapter 3, another typical finding in electroporation research is that the combination of a strong, short pulse (HV) with one or several weak, long pulses (LV) can enhance the TE greatly when compared with using HV or LV alone [1, 2, 4, 28, 94, 81]. In addition, the longer the second pulse, the greater the TE [81]. This trend can be naturally explained from the translocation perspective: the HV is mainly responsible for creating the pores, whereas the LV assists DNA translocation electrophoretically. The above arguments suggest that the translocation theory warrants further examination. In particular, the development of a predictive model is much needed, such as to generate quantitative data to directly correlate with experimental observations.

In this chapter, a stochastic model to study DNA translocation across an electropore driven by finite-time electric pulses is presented. The model is based on previous developments [50, 76, 82] which were primarily used to study DNA sequencing with synthesized or protein nanopores. The model is capable of predicting the probability of successful translocation (PST) as a function of field strength, pulse length, and DNA size. Furthermore, many important insights are revealed, including the effects of the electrophoretic and the diffusive time scales, and a power-law correlation between the final probability of successful translocation (F-PST) and the governing parameters. The simulated results are compared with previous data to interpret the trends. In particular, the diffusive time scale is used to explain the frequency dependence observed in electroporation experiments with uni- and bi-polar pulse trains. Most importantly, this work generates quantitative data which can be tested and validated with well-designed experiments, to further our understanding of the physical processes governing DNA electrotransfer. This work has been published in *BBA Biomembranes* [101].

Abbreviation	Definition
TE	transfection efficiency
PST	probability of successful translocation
F-PST	final probability of successful translocation
PDF	probability density function
PUT	probability of unsuccessful translocation

Table 4.1: Abbreviations used in Chapter 4

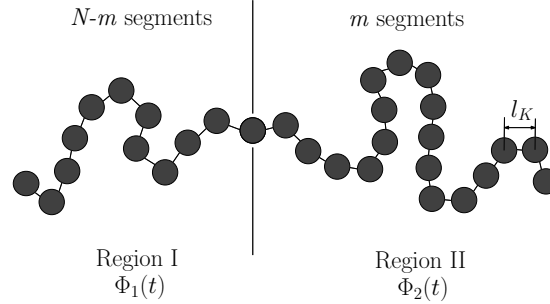


Figure 4.1: A schematic of the problem. The membrane is an infinitesimally thin plane separating region I (the extracellular space) and region II (the intracellular space). The electric potential in each region is denoted by  $\Phi$ .

## 4.2 Model formulation

A schematic describing the physical problem is shown in Fig. 4.1. The membrane is modeled as an infinitesimally thin plane separating two regions, namely, I and II. A pore is embedded on the membrane. The electric potentials of regions I and II are  $\Phi_1(t)$  and  $\Phi_2(t)$ , respectively. Note that  $\Phi_1(t)$  and  $\Phi_2(t)$  are spatial constants, leading to a discontinuity known as the TMP,  $V_m = \Phi_1 - \Phi_2$ . The DNA molecule is modeled as a charged polymer chain consisting of  $N$  segments, each with the Kuhn-length,  $l_K$  (100 nm for double-strand DNA, see Table 4.2) [91]. The polymer chain translocates through the pore as a single strand, i.e., hairpin structures are not considered [39]. The number of segments in region II (the intracellular space) is denoted  $m$ . Correspondingly, the number of segments in region I is  $N - m$ . In each region, the chain is assumed to be a random walk of  $m$  (or  $N - m$ ) segments pinned at the pore on one end. At each instant, the chains are at thermodynamic equilibria.

Our model follows that of Sung *et al.* [82], which was initially used to simulate the translocation of a polymer through a membrane pore under a constant potential

difference. This model has been subsequently developed by Muthukumar and other authors [50, 76]. The above problem can be described by a one-dimensional Fokker-Planck equation governing the evolution of the probability density function (PDF),  $P$ .

$$\frac{\partial P(m, t)}{\partial t} = \frac{\partial}{\partial m} \left[ \frac{k_0}{k_B T} P(m, t) \frac{\partial f(m, t)}{\partial m} + k_0 \frac{\partial}{\partial m} P(m, t) \right]. \quad (4.1)$$

Here  $P(m, t)$  is the probability density of having  $m$  segments in region II at time  $t$ . The probability of having  $N$  segments in region II is the probability of successful translocation.  $k_B$  and  $T$  are the Boltzmann constant and temperature, respectively.  $k_0$  is the effective rate of change coefficient, and is given by the formula:

$$k_0 = \frac{D_0}{L^2}, \quad L = \frac{0.918 l_k}{N^{0.4}}, \quad (4.2)$$

where  $D_0$  is the effective chain diffusivity during translocation, and  $L$  is a characteristic length derived from the radius of gyration,  $R_g$ .  $f$  is the Helmholtz free energy, and consists of contributions from three parts:

$$\frac{f(m, t)}{k_B T} = (1 - \gamma) \ln(m + 1) + (1 - \gamma) \ln(N - m + 1) + m \frac{\Delta \mu}{k_B T}. \quad (4.3)$$

On the right-hand side of the above formula, the first two terms are the entropic energies of  $m$  and  $N - m$  segments, respectively [11], where  $\gamma$  is a constant (Table 4.2). The third term represents the total electrostatic energy summed for all segments, where

$$\Delta \mu = \begin{cases} \tilde{z}_s e V_m, & \text{if } 0 < t < t_p. \\ 0, & \text{if } t > t_p. \end{cases} \quad (4.4)$$

$\tilde{z}_s$  is an effective charge number per segment,  $e$  is the electron charge,  $V_m$  is the TMP introduced above, and  $t_p$  is the pulse length. Note that our formulation deviates slightly from the previous work in two aspects. First, the effective rate of change coefficient,  $k_0$ , is derived from the chain diffusivity  $D_0$  from a scaling analysis. Second, the effective charge number per segment,  $\tilde{z}_s$  is specified according to previous experimental

Symbol	Definition	Value/Source
$F$	Faraday constant	96485 C/mol
$k_B$	Boltzmann constant	$1.38 \times 10^{-23}$ J/K
$T$	room temperature	298.15 K
$l_K$	the Kuhn-length of ds-DNA	100 nm [91]
$l_{bp}$	DNA base-pair length	0.34 nm
$\gamma$	constant for a self-avoiding chain	0.69 [50]

Table 4.2: List of model parameters in Chapter 4

measurements. The details of the derivations and arguments are found in Appendix B.

Equations (4.1)-(4.4) are solved numerically using a second-order finite-volume method. The convective term in Eq. (4.1) is discretized using an upwind scheme. A Crank-Nicolson algorithm is used to integrate the diffusive term in time. At the ends of the computational domain,  $m = 0$  and  $N$ , absorbing boundary conditions are employed [51, 82]. Namely,

$$P(m = 0, N; t) = 0. \quad (4.5)$$

In adopting Eq. (4.5), we assume that once the chain leaves the pore from either side, it will never return. This assumption is consistent with the fact that the entropic energy drops abruptly when the chain departs from the membrane. The flux at  $m = 0$  is collected, which we term the probability of unsuccessful translocation (PUT). The flux at  $m = N$  is collected and termed the probability of successful translocation (PST).

For initial condition, we assume a narrow-band Gaussian distribution approximating a delta function and satisfying the normalization condition  $\int_0^N P(m, t = 0) dm = 1$ . For most of the cases studied below, the center of the initial profile is located at  $m_0 = 0.2$ . The standard deviation of the Gaussian distribution is chosen to be 0.05. In choosing this initial condition, the assumption that a small fractional segment of the polymer chain is already inserted into the pore is made. Other initial locations ( $m_0 = 0.1, 0.5, 1$ , and  $1.5$ ) are also studied to examine the effects of initial condition in Section 4.3. All model parameters are listed in Table 4.2.

### 4.3 Results

In what follows, results are first presented using a DNA polymer chain of  $N = 24$ , which approximately corresponds to a linear length of 7.2 kbp. The initial location is assumed to be at  $m_0 = 0.2$ . The effects of DNA length and initial location are studied later.

Figure 4.2 demonstrates the typical evolution of the PDF,  $P(m, t)$ , subject to a TMP of  $V_m = 0.2$  V and a pulse length of  $t_p = 5$  ms. The pulsing parameters are chosen according to the experiments from Sukharev *et al.* [81] and a comparison with the data is presented later. During the pulse (Figs. 4.2a-c), the peak spreads by diffusion, and is pushed towards the right under the influence of the electrophoretic force. After the pulse ceases, the profile experiences diffusion only and spreads further towards the ends of the domain (Fig. 4.2d). At each instant, the PUT and the PST are collected and their values are presented at the artificial nodes of  $m = -1$  and 25, respectively. However, they are only large enough to be visible in Fig. 4.2d. At a sufficiently long time, the PDF will become uniformly zero (not shown) due to the absorbing boundary conditions, and the sum of the PUT and the PST will reach one.

In Fig. 4.3, the results for a longer pulse of  $t_p = 20$  ms are shown. All other parameters are identical to those used in Fig. 4.2. In contrast to Fig. 4.2, the electrophoretic force drives the PDF peak towards the right (Figs. 4.3a-c) until it reaches the end of the domain (Fig. 4.3d). At  $t = 15$  ms, the PST is already reaching one. For this case, the longer pulse ensures the definitive success of translocation.

The evolution of the PST is more clearly shown in Fig. 4.4, where it is plotted as a function of time for the two cases studied above. For  $t_p = 5$  ms, the PST is very small at the end of the pulse. Indeed, as indicated in Fig. 4.2c, at this time the PDF is centered at around  $m = 11.75$ . Most of the PST increment occurs by the slow diffusive process post-pulsation. This time scale is much longer (seconds) when compared with the pulse length. On the other hand, for  $t_p = 20$  ms, it is observed that the PST increases sharply to one when the pulse is still present. Fig. 4.4 demonstrates that two time scales may manifest during the translocation process. If the pulse is not able to

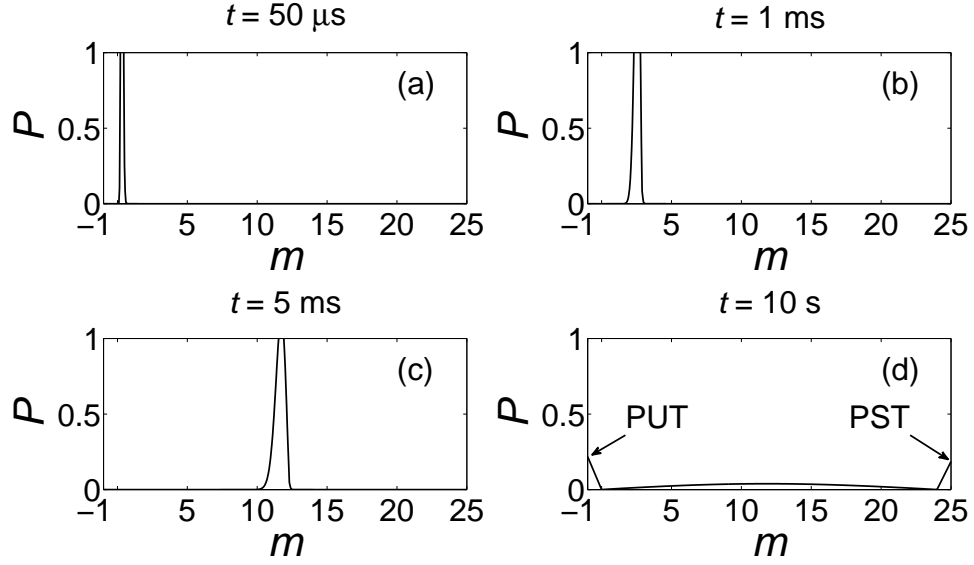


Figure 4.2: Evolution of the PDF,  $P(m, t)$ , for a DNA chain of  $N = 24$ . The initial location is  $m_0 = 0.2$ , the TMP is  $V_m = 0.2$  V and the pulse length is  $t_p = 5$  ms. In Fig. 4.2d, the PUT and the PST are indicated at the artificial nodes of  $m = -1$  and  $25$ , respectively.

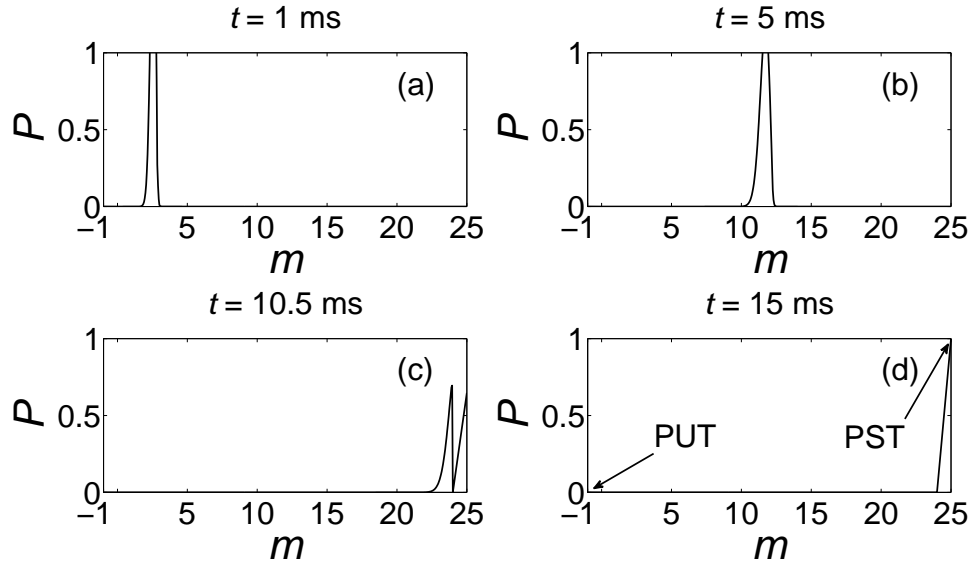


Figure 4.3: Evolution of the PDF,  $P(m, t)$ , for a pulse length of  $t_p = 20$  ms. All other parameters are identical to those used in Fig. 4.2.

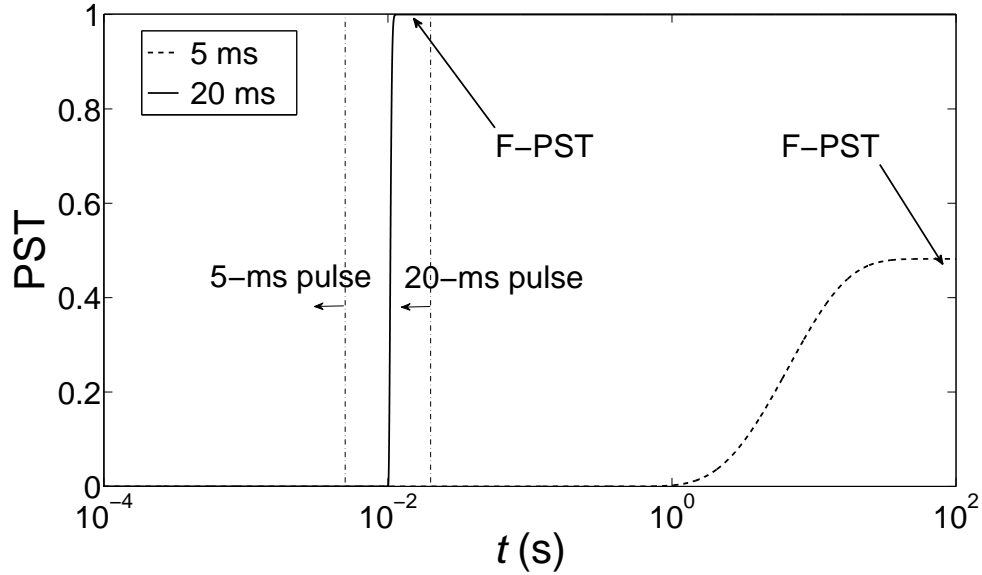


Figure 4.4: Evolution of the PST for the cases studied in Figs. 4.2 and 4.3. The end of the pulse is marked by dash-dotted lines. The final probability of successful translocation (F-PST) is defined as the value of the PST when it reaches the final steady state and is indicated.

completely translocate the chain during its presence, then translocation occurs on the slow diffusive time scale (seconds). On the contrary, if the pulse is sufficiently long, then translocation occurs on the much shorter electrophoretic time scale (ms).

For both of the cases in Fig. 4.4, the PST reaches a steady-state value given sufficient time. This value is termed the “final probability of successful translocation” (F-PST), and its dependence on the pulse length is examined in Fig. 4.5. In addition to  $V_m = 0.2$  V, two other cases, namely,  $V_m = 0.4$  and  $0.6$  V are also studied. For each value of the TMP, the F-PST increases until it saturates at a value very close to 1. Furthermore, the F-PST increases along with an increasing TMP. This trend is examined in detail in Fig. 4.6, where the contours of the F-PST is shown in the phase space of  $V_m$  and  $t_p$ . The contour lines are linear and parallel, with slopes close to  $-1$ , suggesting that to reach the same value of the F-PST,  $V_m$  and  $t_p$  obey a reciprocal correlation. In other words, the product of  $V_m$  and  $t_p$  is constant along the contours. For the contour of  $\text{F-PST} = 0.99$ ,  $V_m \times t_p \approx 2.23$  V $\cdot$ ms. The latter value can be used to define a threshold of pulsing parameters for successful DNA delivery.



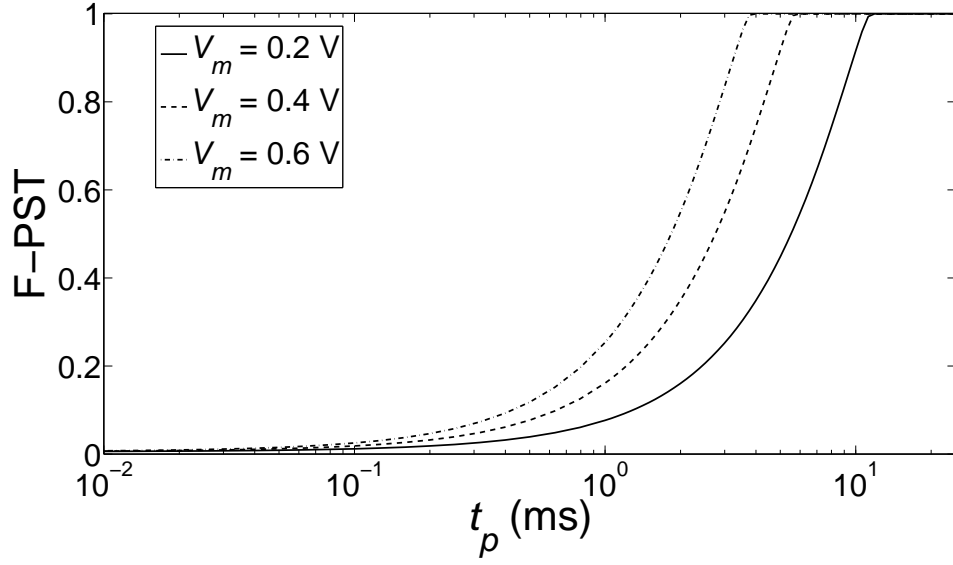


Figure 4.5: The F-PST as a function of the pulse length,  $t_p$ , for  $V_m = 0.2, 0.4$ , and  $0.6$  V. Other parameters are identical as those used in Fig. 4.2.

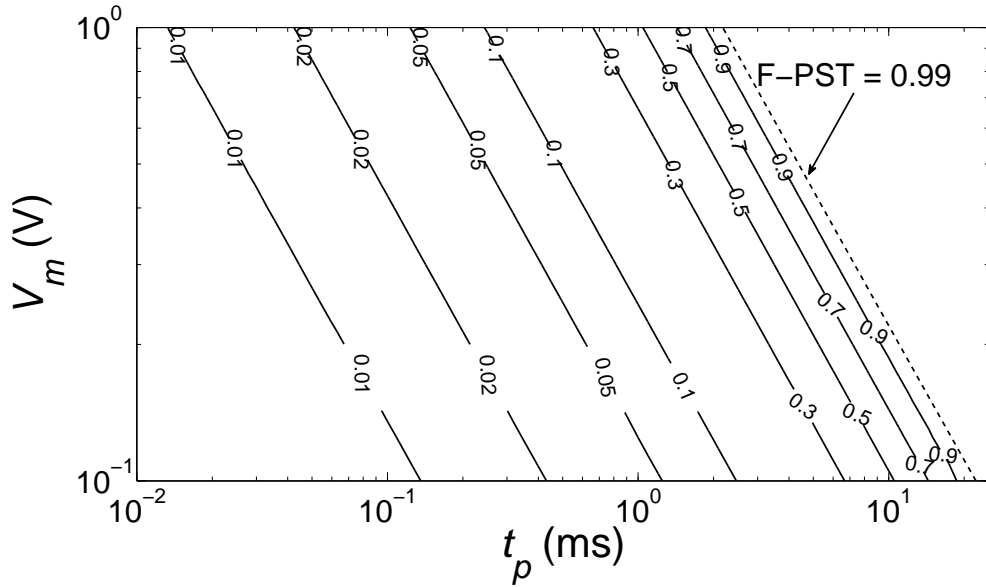


Figure 4.6: Contour plot of the F-PST in the phase space of the TMP ( $V_m$ ) and the pulse length ( $t_p$ ). The slopes for the contour lines are approximately -1, indicating that  $V_m \times t_p \approx \text{Constant}$ .

Here the reciprocal relation between  $V_m$  and  $t_p$  reflects that electrophoresis is the main driving mechanism for translocation. In fact, the F-PST depends strongly on the peak position of the PDF at the end of the pulse. The distance that the peak travels is simply proportional to the product of the electrophoretic velocity and time. Because the drifting velocity has a linear dependence on the TMP (see Eqs. (4.1)-(4.4)), the behavior above is observed.

The effect of DNA size on the F-PST is next examined in Fig. 4.7. In Fig. 4.7a, the F-PST is plotted as a function of the DNA segment number,  $N$ , for  $t_p = 5, 10$ , and 20 ms. The F-PST in general decreases as  $N$  increases and  $t_p$  decreases. The correlation between the F-PST and  $N$  is close to a power law,  $\text{F-PST} \sim N^{-1.5}$ . In Fig. 4.7b, the F-PST is shown as contours in the phase space of  $N$  and  $t_p$ . The contour space lines are again linear and parallel, with slopes close to 0.75, suggesting a power-law correlation between  $N$  and  $t_p$ .

The results from Figs. 4.6 and 4.7 together suggest a similarity behavior of the F-PST as a function of  $V_m$ ,  $t_p$ , and  $N$ . 568 simulations are run with  $V_m$  ranging from 0.1 to 1 V,  $t_p$  from 0.01 to 100 ms, and  $N$  from 17 to 134 (corresponding to DNA sizes from 5 kbp to 40 kbp). The data is shown in Fig. 4.8a and is well-fitted with the correlation,

$$\text{F-PST} = C \times \frac{(V_m t_p)^a}{N^b}, \quad (4.6)$$

where  $C = 45.0$ ,  $a = 1.1$ , and  $b = 1.46$ . These constants are obtained by minimizing the fitting error. The coefficient of determination is  $R^2 \approx 0.999$ , indicating that the formula (Eq. (4.6)) accurately captures the data trend.

In generating the previous results, it is assumed that  $m_0 = 0.2$ . This initial location corresponds to the electrophoretic insertion induced by a prior pulse of  $V_m = 1$  V and  $t_p = 18.5 \mu\text{s}$ . This pulse is comparable to the first 10- $\mu\text{s}$  strong pulse (HV) used in Sukharev et al. [81]. In Fig. 4.8b, the effect of a varying  $m_0$  is studied. The simulations for  $m_0 = 0.1, 0.5, 1$ , and 1.5 are run for the same range of  $V_m$ ,  $t_p$ , and  $N$  values considered in Fig. 4.8a. For each value of  $m_0$ , 106 cases are studied. It is found that the

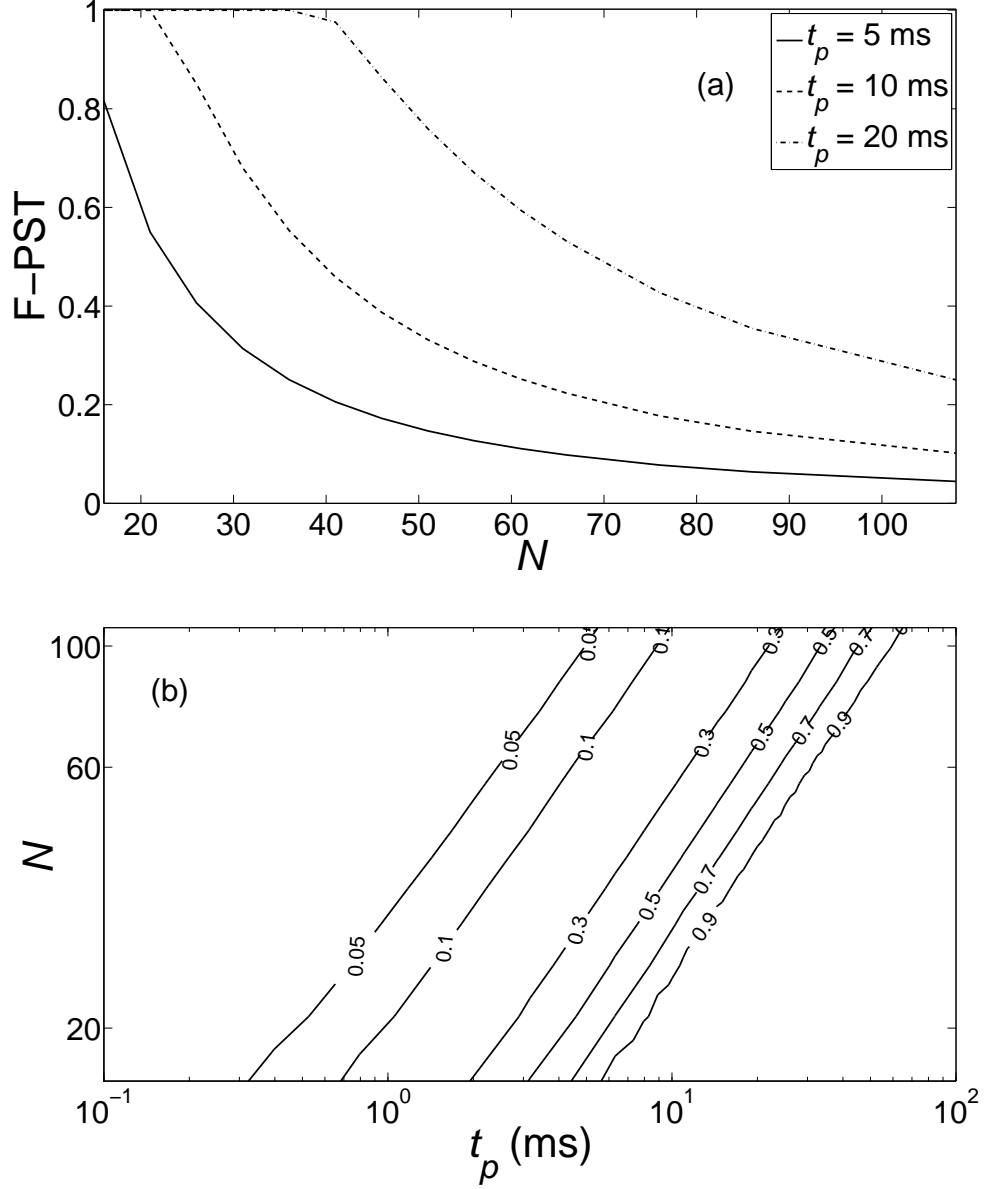


Figure 4.7: The effect of DNA size on translocation probability. (a) The F-PST as a function of the DNA segment number,  $N$ , for  $t_p = 5, 10$ , and  $20$  ms. The descending part of the curves follows approximately the correlation,  $\text{F-PST} \sim N^{-1.5}$ . (b) Contour plot of the F-PST in the phase space of  $N$  and  $t_p$ . The contours are straight and parallel lines following the approximate correlation  $N \sim t_p^{0.75}$ .

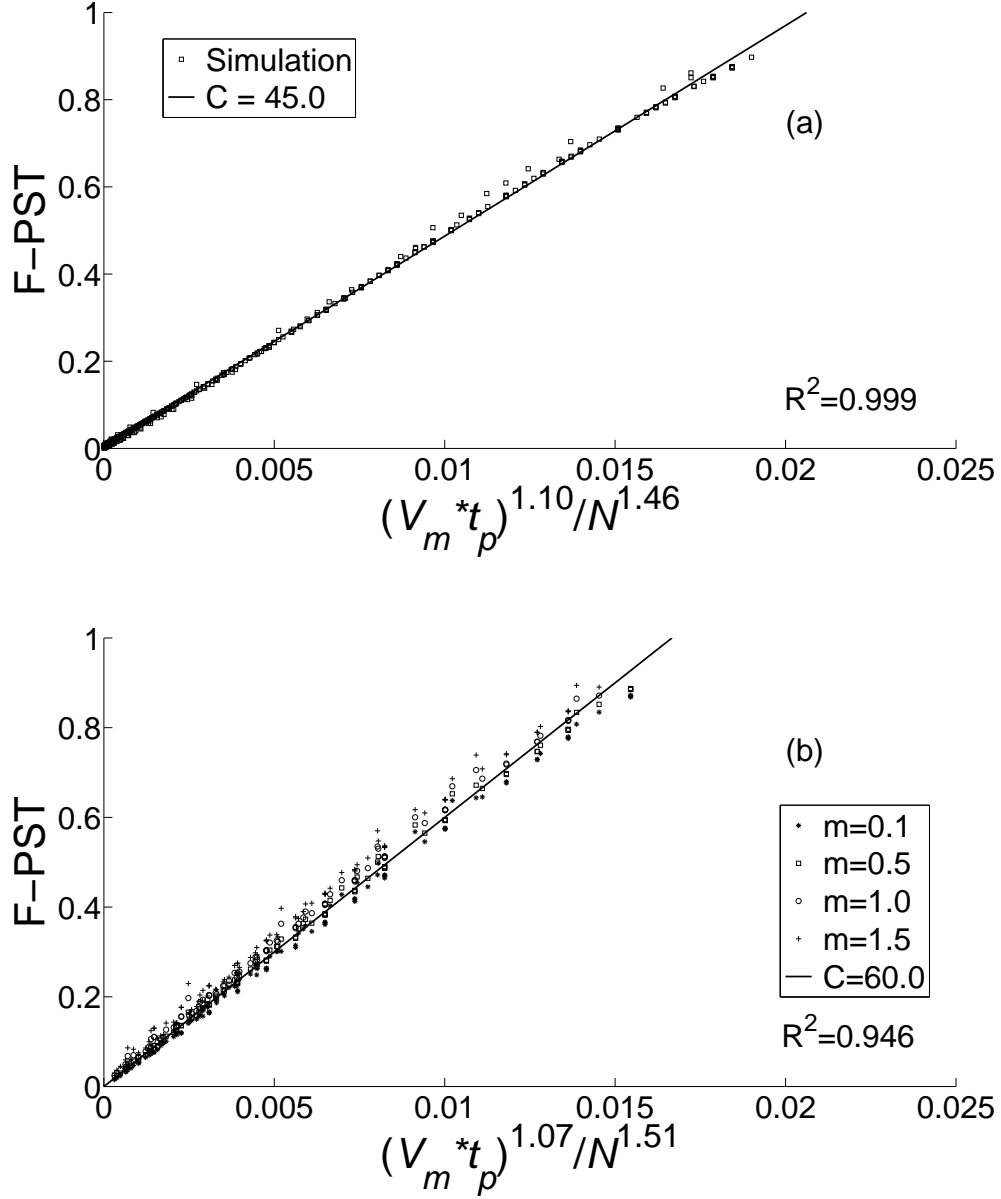


Figure 4.8: The similarity behavior of the F-PST as a function of  $V_m$ ,  $t_p$ , and  $N$ . (a)  $m_0 = 0.2$ . The squares represent simulated results for  $V_m$  ranging from 0.1 to 1 V,  $t_p$  from 0.01 to 25 ms, and  $N$  from 17 to 134. The solid line is a least-square fit,  $F-PST = 45.0 \times (V_m * t_p)^{1.10} / N^{1.46}$ . The coefficient of determination is  $R^2 = 0.999$ . (b) The similarity behavior is also observed for  $m_0 = 0.1, 0.5, 1$ , and  $1.5$ . The simulation is run for the same parametric range as in Fig. 4.8a, and for  $m_0 = 0.1, 0.5, 1$ , and  $1.5$ , the collection of data is best-fitted with the correlation  $F-PST = 60.0 \times (V_m * t_p)^{1.07} / N^{1.51}$  (solid). The coefficient of determination is  $R^2 = 0.946$ .

change in  $m_0$  does not cause appreciable deviation from the power-law behavior. The collection of data is best-fitted with the correlation,  $\text{F-PST} = 60.0 \times (V_m t_p)^{1.07} / N^{1.51}$ . The powers  $a$  and  $b$  only slightly differ from those in Fig. 4.8a, and the coefficient of determination is  $R^2 = 0.946$ . It is worthwhile to mention as  $m_0$  becomes large, eventual departure from Eq. (4.6) is expected (not shown). However, the focus of this work is studying DNA translocation with only a small segment initially inserted.

#### 4.4 Comparison with Experiments

Direct, quantitative comparison with experimental data is difficult due to the lack of sufficient details in the previous measurements. In what follows, the qualitative trends from our simulation and two of the most relevant experimental studies in the literature, namely, by Sukharev *et al.* [81] and Faurie *et al.* [15], are compared and discussed.

The study performed by Sukharev *et al.* used a two-pulse scheme to electroporate simian Cos-1 cells. The first pulse is 6 kV/cm in strength and 10  $\mu\text{s}$  in duration. After a 100- $\mu\text{s}$  delay, a second pulse of 0.2 kV/cm was applied with the duration varying between 0 and 10 ms. The TE was obtained as a function of the second pulse duration (see inset of Fig. 4.9). In general, a near linear dependence is observed. The simulated result using the current model is shown in Fig. 4.9, which is generated following the setup in Section 4.3. The initial PDF is centered at  $m_0 = 0.2$ , and only the second pulse from the experiment is considered. By using this configuration, it is assumed that the first pulse is mainly responsible for pore creation, and the initial insertion of the DNA into the pore. The average DNA length is 7.2 kbp, or  $N = 24$ . The TMP is  $V_m = 0.2$  V which is obtained via the formula  $V_m = 1.25ER$  [31], where  $E = 0.2$  kV/cm is the applied field strength of the second pulse, and  $R = 8\mu\text{m}$  is the cell radius. The simulated F-PST is plotted as a function of the pulse length,  $t_p$ , in Fig. 4.9. Although the F-PST and the TE are not the same, they are both measures for the efficacy of DNA delivery, and comparable linear trends are found in the simulation and the experimental data in Fig. 4.9. Previous theory proposed that the increase in TE was induced by increased pore size and population, or increased permeabilized area due to prolonged field exposure [77]. Here an alternative interpretation is offered

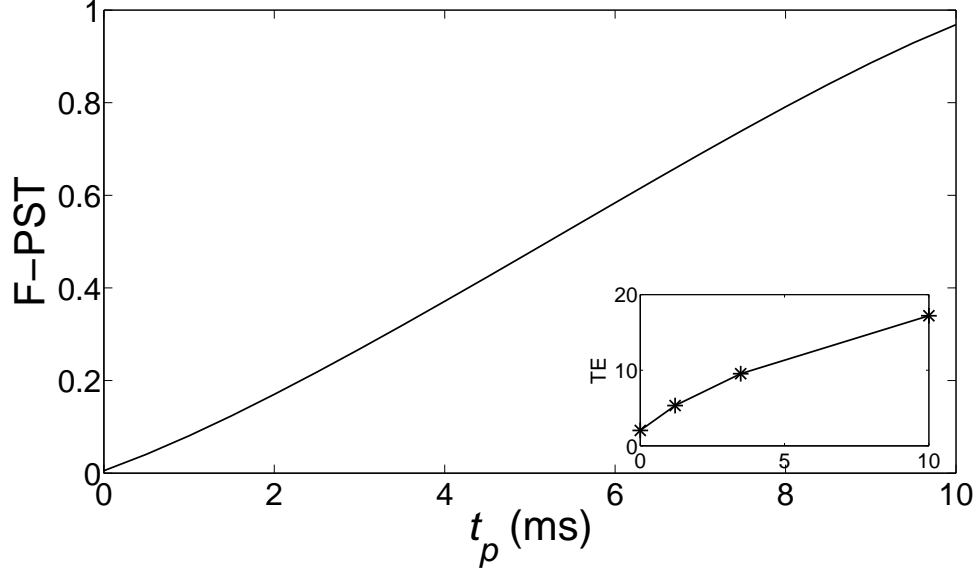


Figure 4.9: Simulated F-PST as a function of  $t_p$  using parameters found in Sukharev *et al.* [81]. The inset shows the original experimental data (stars) in terms of the TE measured by fluorescent intensity.

that longer pulses enhance the probability of translocation, which manifests itself as enhancement in TE.

Next, the experimental data by Faurie *et al.* [15] is examined. In these experiments, a train of six uni-directional (uni-polar) or alternating (bi-polar) pulses were applied to transfect CHO cells with plasmids of 4.7 kbp in average length. Each pulse was 1 ms in duration, with the delay of 0.013, 0.1, 1, and 10 seconds, corresponding to repetition frequencies of 77, 10, 1, and 0.1 Hz, respectively. The resulting fluorescence per cell is shown in Fig. 4.10a.

The simulated results with  $m_0 = 0.2$ ,  $N = 16$ , and the same pulsing scheme as in Faurie *et al.* are presented in Fig. 4.10b. Although there are noticeable differences between the data and the simulation, the latter captures a few important features of the former. For the uni-polar pulse, the simulation predicts a curve with the similar shape to that in the experimental data. The F-PST begins to increase at approximately 1 Hz. For frequencies greater than 1 Hz, the F-PST reaches one asymptotically, suggesting a high probability of successful delivery. For the bi-polar pulse, the simulation captures

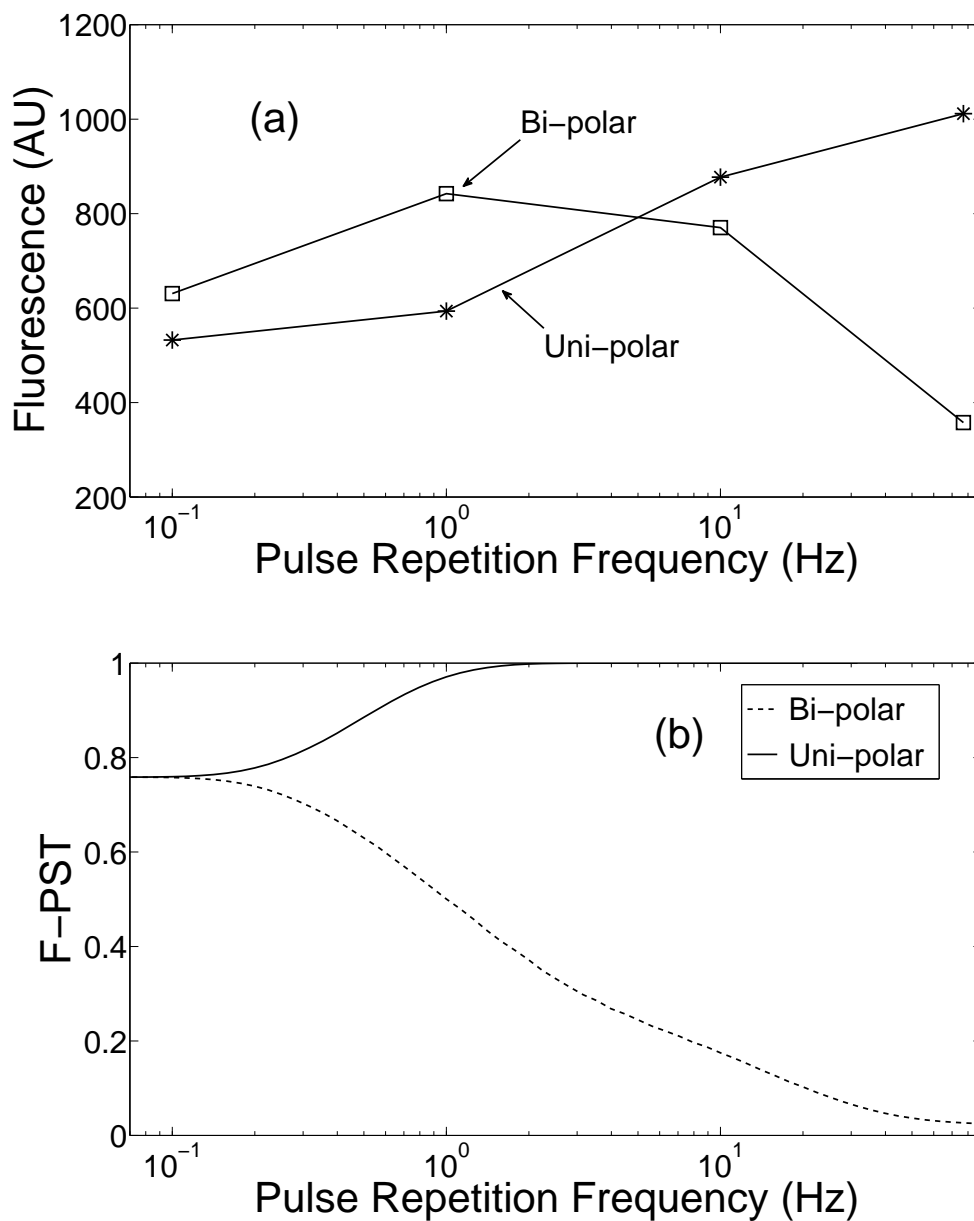


Figure 4.10: (a) Experimental results from Faurie et al. [15]. The fluorescence intensity per viable cell is plotted as a function of the pulse repetition frequency. (b) Simulated result using parameters from the experiment.

the descending trend for frequencies higher than 1 Hz.

The main difference between the data and the simulation is at the lower frequencies. In the experiments, the bi-polar pulse results in a TE higher than the uni-polar one, whereas in the simulation, these two pulsing schemes lead to similar values of the F-PST. This effect is possibly attributed to the fact that DNA molecules can enter the cell from both sides under bi-polar pulses [14], enhancing the probability of delivery. This mechanism is not included in the current model, and is also likely responsible for the peak at 1 Hz shown in Fig. 4.10a.

The frequency dependence in the simulation is mediated by a diffusive time scale, which is argued here to be responsible for the trends observed in the experimental data. As demonstrated in Section 4.3, if a single pulse is not able to complete the translocation by electrophoresis, then the translocation (either successful or unsuccessful) is governed by the diffusive drifting of the polymer chain post-pulsation. For the plasmids considered in Faurie *et al.*, this time scale is  $R_g^2/D_0 = 5.5$  s, using  $R_g = 250$  nm, and  $D_0 = 1.13 \times 10^{-14}$  m<sup>2</sup>/s. At low frequencies, the sufficient delay time between pulses ensures that the translocation is completed, such that there's no compounding effect between the individual pulses. For this case, the uni- and bi-polar pulses do not behave differently according to the model, although in reality the effect noted above may render the bi-polar pulse more advantageous. As the frequency increases and the delay time decreases below the threshold, additional uni-polar pulses help push-in the plasmids into the cell, whereas bi-polar pulses tend to reverse the translocation, hence causing the observed behavior.

However, it should be emphasized that in the experiments and between the pulses, diffusive drifting of the chain may not be the only mechanism at work. Endocytosis can be triggered at this stage, and the direct interaction of the DNA molecule and the membrane may also play a role. The complete intake of DNA may thus be a complex process involving all these aspects. On the other hand, regardless of the specific nature, the mechanism(s) needs to act on the characteristic time scale of a few seconds to be able to explain the frequency dependence observed.

Finally, it is worthwhile to remark that although the above comparisons are only



qualitative, our theory can be verified with well-designed quantitative experiments. For example, experiments similar to those by Sukharev *et al.* can be repeated, but with a wider and controlled range of  $V_m$ ,  $t_p$  and  $N$  values to validate the similarity behavior indicated by Eq. (4.6). In particular, pulses with the same product,  $V_m \times t_p$ , should result in similar values of TE. For uni-polar and bi-polar pulsing experiments, different sizes of plasmids can be used which leads to different diffusive time scales, such that they may be detected in the measurements. In addition, the length of each individual pulse can also be explored as a control parameter, such that the electrophoresis-dominant and diffusion-dominant regimes can be differentiated.

#### 4.5 Conclusions

In this work, a 1D Fokker-Planck simulation for the translocation of a DNA polymer through a membrane-bound nanopore is presented, within the context of electroporation-mediated molecular delivery. The model provides a few important insights.

- The translocation may occur on two disparate time scales, namely, the electrophoretic time ( $\sim$  ms), and the diffusive time ( $\sim$  s). If the pulse is sufficiently long to complete the translocation via electrophoretic drifting, then the electrophoretic time scale is observed. Otherwise, translocation completes (either successfully or unsuccessfully) on a much longer diffusive time.
- The F-PST (the final probability of successful translocation) follows the correlation,

$$\text{F-PST} \sim \frac{(V_m t_p)^a}{N^b}.$$

The values of  $a$  and  $b$  are close to 1 and 1.5, respectively, for small  $m_0$ -values, or for DNA chains with small initial insertion distances. The dependence of the F-PST on the product,  $V_m \times t_p$ , directly reflects that translocation is primarily driven by electrophoretic drifting.

The simulation results are compared with experimental data from previous studies. In particular, the diffusive time scale is proposed to explain the frequency dependence

observed in electroporation experiments with uni- and bi-polar pulse trains. Another important contribution of the work is that the model predicts trends and correlations (such as Eq. (4.6)) that can be verified with well-designed experiments.

## Chapter 5

### A preliminary study of vesicle/cell relaxation

#### 5.1 Introduction

Complex responses are induced when cells and vesicles are exposed to applied electric fields. Besides the phenomenon of electroporation, cell electrodeformation and relaxation is another class of important problems in biological research. In particular, quantitative measurements of cell electrodeformation can be used as a technique to probe membrane properties [36]. This topic has been of our particular interest, as changes in biomechanical and biophysical properties of cells are closely related to the onset and progression of human diseases [83]. For example, human breast cancer cells are "softer" than healthy breast cells, and they become even more deformable in metastatic state [23]. On the other hand, human hepatocellular carcinoma cells exhibit greater stiffness when compared with normal hepatocytes [102]. The research field of biomechanics has seen a rapid growth in the past decade, with its great potential in developing new biomedical techniques [83].

Previously, Sadik *et al.* [71] performed an experimental investigation of large vesicle electrodeformation with various DC field strengths and intra-to-extra-vesicular conductivity ratios [71]. In a companion work, Zhang *et al.* performed a transient analysis to quantify droplet/vesicle electrodeformation and relaxation [103, 104]. Here relaxation refers to the retraction of a droplet/vesicle back to the original spherical shape when the forcing mechanism is removed. By assuming that the initial spherical droplet/vesicle always stays in a spheroidal shape, Zhang *et al.* analytically derived ODEs that govern the dynamics of aspect ratio change both for electrodeformation and relaxation. The model prediction is found to agree well with the experiments by Riske and Dimova [65], revealing that the vesicle relaxation obeys a universal behavior regardless of the means

of deformation. This is one of the most important contributions of Zhang et al's work [104], as the universal scaling law provides a simple approach to detect membrane properties by studying vesicle/cell relaxation, instead of deformation which is presumably a much more complex process.

In this work, the author implements a small-deformation analysis to reveal important physical insights of our theory that was not clearly understood previously. The author then extends our model investigation to a practical use, namely, directly extracting membrane properties from time-resolved measurements of aspect ratio change during relaxation. The importance of this work lies in developing a simple but reliable method of detecting well-defined mechanical properties of any vesicle/cell group. This work is currently under preparation for a journal publication.

## 5.2 A small-deformation analysis of vesicle relaxation

In our previous work [104], the governing equation for vesicle relaxation is derived within the prolate spheroidal coordinate system. This result is in general valid from the regime of small- to moderate-deformation, which has been verified through comparison with experimental data. Nevertheless, one limitation of this theory is that the resulting solution assumes a relatively complex mathematical form. This limitation poses challenges in understanding the physical mechanisms governing the process. Here we pursue a simplification by performing a small-deformation analysis of the problem. Through investigation of the system behavior, the author proves that the governing equation in [104] (Eq. 37 therein) converges to that for droplet relaxation in the leading order, or equivalently in the limit of infinitesimally small-deformation. The details of derivation are provided in the following, and a brief discussion is presented in the end of this section.

### 5.2.1 Problem description

A schematic of the problem is shown in Fig. 5.1. A vesicle formed by an infinitesimally thin membrane is suspended in another fluid. The intra- and extra-vesicular viscosities

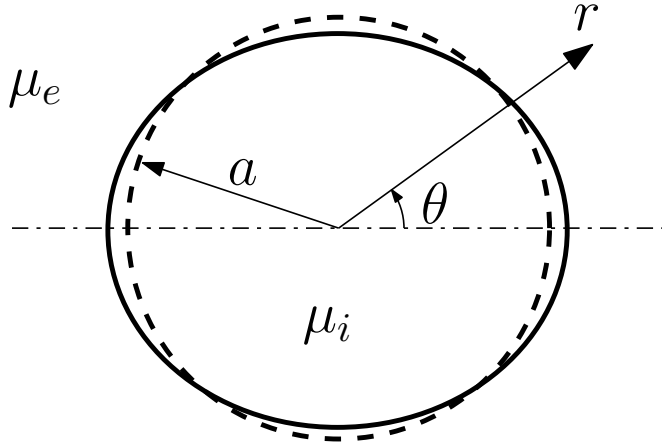


Figure 5.1: A schematic of the problem.

are  $\mu_i$  and  $\mu_e$ , respectively. The vesicle membrane is subject to a uniform tension of  $\Gamma_0$  at rest, and the vesicle remains in a spherical shape without any external force applied (the dashed line in Fig. 5.1). To solve the relaxation problem, it is assumed that the vesicle has been pre-deformed into a prolate spheroidal shape of aspect ratio  $e_0$ , which is defined as the ratio of the major axis to the minor axis of the spheroid (the solid line in Fig. 5.1). At the beginning of this problem, or the time  $t = 0$ , the application of all external deforming forces (e.g., electrical forces) has been removed and all residual effects have also vanished. In other words, the relaxation process does not depend on any detail of how the vesicle was deformed. This assumption is always a good one as long as the relaxation process is the slowest one compared to any residual effect of the deformation process (e.g., membrane discharging in electrodeformation).

The problem is solved within an axisymmetric spherical coordinate  $(r, \theta)$  as shown in Fig. 5.1. To obtain a small-deformation solution,  $e_0 - 1 \ll 1$  is presumed and all the derivation is based on the leading-order Taylor expansion of each term with respect of  $e - 1$ . The intra-vesicular fluid is assumed to be incompressible such that the volume of vesicle is a constant throughout the relaxation process.

### 5.2.2 The hydrodynamic problem

Dimension analysis shows that the Reynolds number of the problem is of the order  $\tau_{diff}/\tau_{relax}$ , where  $\tau_{diff} = a^2/\nu$  is the diffusive time scale, and  $\tau_{relax} = \mu a/\Gamma_0$  is the relaxation time scale. Experiments show that [65],  $\tau_{relax}$  is of the order of milliseconds to seconds depending on magnitude of  $\Gamma_0$ , which is much longer than  $\tau_{diff}$  which is in the order of microseconds in this problem. Consequently, the Stokes equation for an incompressible flow is used here to solve the flow problem, which can be rewritten in terms of the stream function,  $\psi$ , as:

$$\nabla^4 \psi_{i,e} = 0. \quad (5.1)$$

The subscript  $i$  and  $e$  denote intra- and extra-vesicular space, respectively. In the spherical coordinate system, the relationships between  $\psi$  and velocity/pressure are:

$$u_r = \frac{1}{r^2 \sin \theta} \frac{\partial \psi}{\partial \theta}, \quad u_\theta = -\frac{1}{r \sin \theta} \frac{\partial \psi}{\partial r}, \quad (5.2)$$

$$-\nabla p + \mu \nabla^2 \mathbf{u} = 0. \quad (5.3)$$

$u_r$  and  $u_\theta$  are radial and polar components of velocity vector  $\mathbf{u}$ , respectively, and  $p$  is the pressure. Once  $\psi$  is solved from Eq. (5.1), the expression of intra- and extra-vesicular velocity/pressure can be found through Eqs. (5.2) and (5.3).

### 5.2.3 Boundary conditions

Without any external forces applied, the velocity field converges to zero at infinity. It also has to be finite at  $r = 0$ . At the membrane, the following conditions are applied:

$$\mathbf{u}_i = \mathbf{u}_e, \quad (5.4)$$

$$\mathbf{u}_i \cdot \mathbf{n} = \mathbf{u}_e \cdot \mathbf{n} = u_n, \quad (5.5)$$

$$\int_S u_n \cdot (T_{nn}^e - T_{nn}^i - f_n^{mem}) dS = 0, \quad (5.6)$$

$$T_{nt}^e = T_{nt}^i. \quad (5.7)$$

Equation (5.4) is the velocity continuity condition across the membrane. Equation (5.5) is the kinematic condition which relates the normal velocity  $u_n$  of the membrane to the rate of aspect ratio change. The details are presented in Section 5.1.5. Equations (5.6) and (5.7) refers to the normal and tangential stress matching condition, respectively. Here  $T$  denotes components of the hydrodynamic stress tensor,  $\mathbf{f}^{mem}$  denotes the force density arising from the membrane, and subscripts  $n$  and  $t$  denote the components in the normal and tangential direction, respectively. Note that in Eq. (5.6) a global balance integrated over the whole membrane surface is used instead of a point-to-point balance, which is not possible to be established with a uniform distribution of  $\mathbf{f}^{mem}$  in the current problem.

According to [104], the membrane force density  $\mathbf{f}^{mem} = 2\Gamma H\mathbf{n}$ , where  $\Gamma$  is the local membrane tension and  $H$  is the mean curvature. In case that the deformation is not extremely large, the correlation between  $\Gamma$  and aspect ratio  $e$  arises from the folding and unfolding of molecular-level thermal undulation [26], which is governed by:

$$\Delta(e) = \frac{k_B T}{8\pi\kappa} \ln \frac{\Gamma}{\Gamma_0}, \quad (5.8)$$

where  $k_B$  is the Boltzmann constant,  $T$  is the temperature and  $\kappa$  is the bending rigidity of the membrane. The dimensionless function  $\Delta$  is the increase in apparent membrane area of a spheroid relative to the spherical state:

$$\Delta = \frac{1}{2}(1 - \xi_0^{-2})^{-\frac{2}{3}}[1 - \xi_0^{-2} + (\xi_0^2 - 1)^{\frac{1}{2}} \arcsin(\xi_0^{-1})] - 1, \quad (5.9)$$

where  $\xi_0 = (1 - e^{-2})^{-\frac{1}{2}}$ . Equations (5.8) and (5.9) together give the quantitative information of membrane force density as a function of deforming state.

#### 5.2.4 Base state

In solving the problem, the objective is to find out the transient solution for  $e$  in its leading order of Taylor expansion. In other words, the velocity, pressure, stress terms are

in the order of  $e - 1$  or  $\dot{e}$ . This refers to a small deviation from the “base state”, which is the solution corresponding to the spherical state of the vesicle at rest. Equations (5.1)-(5.7) define the governing equations of a complete solution, which is the superposition of the base-state and the small-deformation solution. In the following, a superscript 0 is used to denote the base state, and the variables without superscript 0 as used in all the previous formula, are changed to represent the leading-order small-deformation solution, instead of the complete solution hereafter.

It is straightforward to obtain the solution of the base state:

$$\psi_{i,e}^0 = \text{Constant}, \quad (5.10)$$

$$\mathbf{u}_{i,e}^0 = \mathbf{0}, \quad (5.11)$$

$$p_e^0 = p_\infty, \quad p_i^0 = p_\infty + \Gamma_0 \cdot \frac{2}{a}, \quad (5.12)$$

where  $p_\infty$  is a constant pressure at infinity. Subtracting the contributions of base state from Eqs. (5.1)-(5.7), the governing equations for the small-deformation solution can be obtained. It turns out that all equations keep exactly in the same form except that  $\mathbf{f}^{mem}$  now has a new expression of  $\mathbf{f}^{mem} = (2\Gamma H - \Gamma_0 \cdot \frac{2}{a})\mathbf{n}$ .

### 5.2.5 Kinematic condition

The normal velocity at each point of the membrane  $u_n$  is not an independent variable. It has an intrinsic correlation with the rate of aspect ratio change  $\dot{e}$ . This correlation can be derived by the following approach. The surface equation of a spheroid with an aspect ratio of  $e$  and a volume of  $\frac{4}{3}\pi a^3$  in  $(r, \theta)$  is

$$r - ae^{-\frac{1}{3}}[1 - \cos^2 \theta(1 - \frac{1}{e^2})]^{-\frac{1}{2}} = 0. \quad (5.13)$$

In its leading-order expansion with respect to  $e - 1$ , Eq. (5.13) is simplified to a surface equation:

$$F(r, \theta, e) = r - a[1 - \frac{1}{3}(e - 1)(1 - 3\cos^2 \theta)] = 0. \quad (5.14)$$



From this surface equation, the normal velocity on the membrane can be derived as a function of  $e$  and polar angle:

$$u_n = -\frac{1}{|\nabla F|} \frac{\partial F}{\partial t} = -\frac{1}{3} a \dot{e} (1 - 3 \cos^2 \theta). \quad (5.15)$$

### 5.2.6 Results

To satisfy Eq. (5.15) on the membrane, the leading-order solution of  $\psi$  is assumed to be in the following mode:

$$\psi(r, \theta) = \sin^2 \theta \cos \theta r^n. \quad (5.16)$$

Substituting Eq. (5.16) into Eq. (5.1), it can be solved out that available values of  $n$  are -2, 0, 3 and 5. Considering the constraints at infinity and  $r = 0$ , the solutions of  $\psi$  are:

$$\psi_i = (C \frac{r^3}{a} + D \frac{r^5}{a^3}) \sin^2 \theta \cos \theta, \quad (5.17)$$

$$\psi_e = (A \frac{a^4}{r^2} + B a^2) \sin^2 \theta \cos \theta, \quad (5.18)$$

where A, B, C and D are undetermined constants in the dimension of velocity. Their values are solved by applying the boundary conditions Eqs. (5.4)-(5.7). The mathematical expressions for velocity, pressure and stress terms are presented in Appendix C. The final results of linear equations of A, B, C and D are:

$$\begin{cases} C + D = A + B = \frac{1}{3} a \dot{e} \\ 3C + 5D = -2A \\ \mu_i(8D + 3C) = \mu_e(8A + 3B) \\ \frac{8}{5}[\mu_e(6B + 8A) - \mu_i(D - 2C)] = -\frac{32}{15}(e - 1)\Gamma(e) \end{cases}. \quad (5.19)$$

By eliminating A, B, C and D from Eq. (5.19), the final governing equation of  $e$  can be derived:

$$\frac{de}{d\tau} = -\frac{40(\mu_r + 1)}{(2\mu_r + 3)(19\mu_r + 16)}(e - 1) \exp\left[\frac{8\pi\kappa\Delta(e)}{k_B T}\right], \quad (5.20)$$

where  $\mu_r = \mu_i/\mu_e$  is the intra-to-extra-vesicular viscosity ratio,  $\tau = t/\tau_0$  is the dimensionless time, and the characteristic time  $\tau_0 = \mu_e a/\Gamma_0$ .

Equation (5.20) is the main result of this work, as it connects our general solution in [103, 104] with available analytical solution of droplet relaxation in the small-deformation regime. On one hand, in the case for droplet relaxation, the exponential term on the right-hand side of Eq. (5.20) will be replaced by 1 as the interfacial tension is a constant  $\gamma$  and does not depend on  $e$  (no undulation effect involved). Then Eq. (5.20) will give the same leading-order solution as in [24] (Eq. 3 therein), which makes an analysis for the retraction of a droplet from a deformed shape to the spherical state. This validates our theoretical derivation above.

On the other hand, for  $\mu_r = 1$ , Eq. (5.20) can be simplified and rewritten into the following form:

$$\frac{de}{d\tau} = -\frac{3}{14} \times \frac{32}{15} (e-1) \times \exp\left[\frac{8\pi\kappa\Delta(e)}{k_B T}\right]. \quad (5.21)$$

Compared to our general governing equation in [104] which is also derived assuming  $\mu_r = 1$ :

$$\frac{de}{d\tau} = -\frac{1}{F} (\xi^2 - 1)^{-\frac{3}{2}} f_{24}(\xi_0) \exp\left(\frac{8\pi\kappa\Delta}{k_B T}\right), \quad (5.22)$$

here  $\frac{3}{14}$  and  $\frac{32}{15}(e-1)$  in Eq. (5.21) are the analytical leading-order terms of Taylor expansion of  $\frac{1}{F}(\xi_0^2 - 1)^{-\frac{3}{2}}$  and  $f_{24}(\xi_0)$  in Eq. (5.22) about  $e = 1$  (spherical state), respectively. In other words, Eq. (5.21) is verified to be a leading-order approximation of our general solution in the small-deformation regime.

### 5.2.7 Discussion

The main contribution of this theoretical work is that it proves the following fact: the governing equation for vesicle relaxation converges to that for droplet relaxation in the limit of infinitesimally-small-deformation regime. This behavior can be easily seen from Eq. (5.20), as the leading-order term of Taylor expansion of the exponential term about  $e = 1$  is simply 1 ( $\Delta(e = 1) = 0$ ). This corresponds to a constant membrane tension of  $\Gamma_0$ , analogous to the surface tension coefficient  $\gamma$  for a droplet interface. Given this

behavior, the relaxation of a vesicle close to spherical state is an exponentially-decaying process governed by a single time scale:

$$\tau_{relax} = \frac{(2\mu_r + 3)(19\mu_r + 16)}{40(\mu_r + 1)} \frac{\mu_e a}{\Gamma_0}. \quad (5.23)$$

With  $\tau_{relax}$ ,  $\mu_{i,e}$  and  $a$  measured, then the membrane tension  $\Gamma_0$  can be extracted from well-designed experiments.

Furthermore, Eq. (5.21) which corresponds to the case of  $\mu_r = 1$ , helps reveal important physical insights of different regimes in the relaxation process. In the right-hand side of Eq. (5.22),  $\frac{1}{F}(\xi_0^2 - 1)^{-\frac{3}{2}}$ ,  $f_{24}(\xi_0)$  and the exponential term represent the effect of hydrodynamic dissipation, membrane energy change resulting from local curvature, and thermal undulation, respectively. From an energy point of view, Eq. (5.22) is equivalent to regulating the energy release of a deformed membrane through hydrodynamic dissipation inside and outside the vesicle. The term of  $\frac{1}{F}(\xi_0^2 - 1)^{-\frac{3}{2}}$  appears to depend on  $e$  very weakly (numerical plot shows that this is true even for a relatively large value of  $e$ ), suggesting a “steady” dissipation rate of energy independent of deformation. Consequently, the behavior of relaxation is governed by the competition between  $f_{24}$  and the exponential term.

When  $e$  is close to 1 (small-deformation regime), the change of membrane energy is dominated by the behavior of the second term ( $f_{24}$ ), namely, change of local curvature. Therefore the behavior is similar to that for relaxation of a pure liquid droplet. When  $e$  departs from the small-deformation regime such that the behavior of the exponential term dominates over  $f_{24}$ , a logarithm-like dependence of the aspect ratio on time manifests. Finally, in the moderate-deformation regime, the contributions from  $f_{24}$  and the exponential terms are comparable, which leads to a transition solution between “logarithm-like” and “exponential-decaying” regime. The typical behavior of these three regimes are shown in Fig. 5.2, which is discussed in detail in the next section.

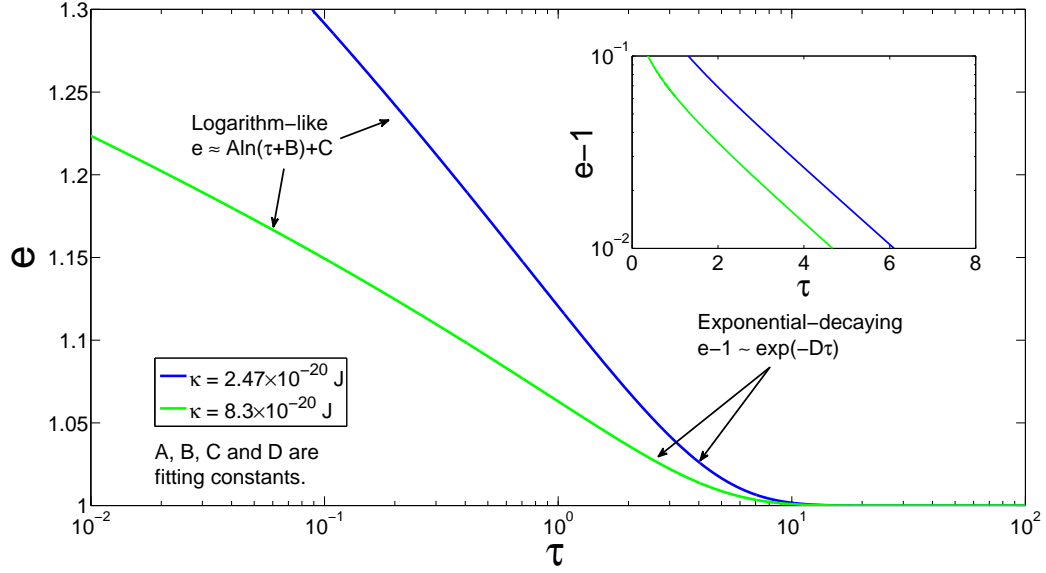


Figure 5.2: Schematic of regimes in vesicle relaxation. Solid curves are numerical solution of Eq. (5.22) for two different values of membrane bending rigidity  $\kappa$ . When the deformation is moderate ( $e > 1.2$  for this case), the aspect ratio shows a logarithm-like dependence on the dimensionless time  $\tau$ . When the deformation is very small ( $e < 1.05$ ), the aspect ratio decays exponentially to 1 (spherical state), and the decaying time scale is independent of  $\kappa$  (inset). There is a transition regime for  $e$  between 1.05 and 1.2, which is not apparently seen in this case.

### 5.3 Extraction of membrane properties

The main goal of this work is to find a simple yet reliable method to extract membrane mechanical properties from experimental measurements. In the current model, two membrane parameters, namely, the bending rigidity,  $\kappa$ , and the initial membrane tension,  $\Gamma_0$ , are involved. From the discussion in Section 5.2,  $\Gamma_0$  can be extracted by measuring the characteristic time scale of relaxation in the small-deformation regime. On the other hand, the bending rigidity,  $\kappa$ , can be extracted from relaxation in the moderate-deformation regime, as shown in Fig. 5.2.

Figure 5.2 plots the numerical solution of Eq. (5.22) for two realistic values of  $\kappa$ , ( $2.47 \times 10^{-20}$  J, blue;  $8.3 \times 10^{-20}$  J, green). The logarithm-like and exponential-decaying regimes for aspect ratio are marked. As demonstrated in the previous section, when  $e < 1.05$ , it shows an exponentially-decaying behavior. The decaying time scale is independent of  $\kappa$ , which is more clearly shown in the inset of Fig. 5.2. When  $e > 1.2$

(moderate deformation), it shows a linear dependence on logarithm of  $\tau$ , which manifests when the behavior of the exponential term dominates in Eq. (5.22). Numerical and theoretical analyses both show that the slope of this "linear behavior" is inversely correlated with  $\kappa$ . Such system characteristics suggest that, the value of  $\kappa$  can be obtained by measuring the "slope" of relaxation from the plot of  $e$  against  $\ln \tau$ .

It is worthwhile to mention that, there is also a transition regime for  $e$  between 1.05 and 1.2. However, in most realistic cases the solution in this regime shows similar behavior as for  $e > 1.2$ , and is therefore not apparently seen in Fig. 5.2.

The values of  $\kappa$  for four different types of vesicles/cells are extracted by fitting the numerical solution of Eq. (5.22) with experimental data following a least-square error principle. The experiments were performed by Riske and Dimova [66] (vesicles) and by Yao and Xiong [87] (breast cancer cells), respectively. The results are shown in Fig. 5.3. The vesicle/cell types are: POPC, vesicle of a lipid membrane of 1-palmitoyl-2-oleoyl-sn-glycero-3-phosphocholine; MCF7, a breast cancer cell line; Egg-PC GUV, Giant unilamellar vesicles of L- $\alpha$ -phosphatidylcholine from egg yolk; MDA-MB-231, a breast cancer cell line in metastatic state.

A surprising observation is that, cell relaxation, although presumably a much more complex problem, shows very similar behavior to vesicle relaxation, and is well captured by our model. More importantly, the MDA-MB-231 cells are found to be "softer" (having a lower value of  $\kappa$ ) than MCF7 by our approach. This agrees with the behavior of metastatic cancer cells which are softer such as to migrate more easily. Our model and approach therefore has the potential to be developed into a simple, reliable and promising tool in detecting mechanical properties for not only vesicles, but also biological cells. This is a significant advance compared to most previous methods, which either adopted over-simplified, coarse-grained models or included so many unnecessary details that the model has become too complex for practical applications.

## 5.4 Conclusions

The main findings of this work are:

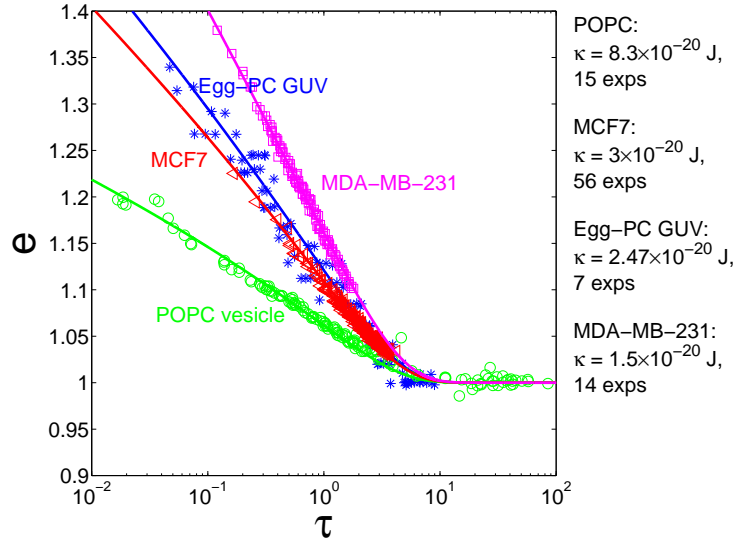


Figure 5.3: Extraction of membrane bending rigidity  $\kappa$  by fitting numerical solution (solid) of Eq. (5.22) and experimental data (symbols), for four different types of vesicles/cells. The vesicle/cell types are: POPC, vesicle of a lipid membrane of 1-palmitoyl-2-oleoyl-sn-glycero-3-phosphocholine; MCF7, a breast cancer cell line; Egg-PC GUV, Giant unilamellar vesicles of L- $\alpha$ -phosphatidylcholine from egg yolk; MDA-MB-231, a breast cancer cell line in metastatic state.

- The author theoretically proves that, in the limit of infinitesimally-small-deformation, vesicle relaxation behaves identically to droplet relaxation. This process is an exponentially-decaying one governed by a single time scale  $\tau_{relax}$ , which is a function of intra- and extra-vesicular viscosities, initial vesicle radius and membrane tension. With viscosities and vesicle radius known, the membrane tension can be extracted by measuring the decaying time scale of vesicle relaxation in the regime of small deformation.
- An intrinsic mechanical property of the membrane, bending rigidity, can be extracted by fitting the model prediction with time-resolved measurement of vesicle relaxation in the regime of moderate deformation. In this regime, the relaxation process is dominated by the membrane energy change due to folding of thermal undulation. This leads to a logarithm-like dependence of the aspect ratio on time. With this approach, membrane properties are extracted for experimental data of two groups of vesicles (egg-PC, POPC) and cells (MCF-7, MDA-MB-231),

respectively. Preliminary results show that the membrane properties of vesicles extracted from our new approach is in good agreement with that from other methods [66]. In addition, the author correctly captures a lower bending rigidity from MDA-MB-231 cells (cancer breast cells in metastatic state) compared to that from MCF-7 cells. This validates our approach as a simple, reliable and promising tool in detecting mechanical properties for not only vesicles, but also biological cells.

## Chapter 6

### Conclusions

In this thesis, the author implemented model studies of electroporation-mediated delivery for three different types of target molecules: propidium iodide, Fluorescein-Dextran and linear double-strand DNA polymer chain. For the first two tasks, molecular delivery are simulated by numerically solving the coupled electrical problem, the ASE model for membrane permeabilization, and the Nernst-Planck Equation for transport. For the third task, a 1D Fokker-Planck simulation is presented for the translocation of a DNA polymer through a membrane-bound nanopore.

In the study of PI delivery, simulated results are directly compared with temporally- and spatially-resolved experiments by Sadik *et al.* [72] to tackle the basic physical processes involved in electroporation-mediated molecular delivery. Through a careful investigation of the process of membrane permeabilization and pore dynamics, a clear and comprehensive physical understanding is established to quantitatively explain experimental observations. In particular, an electrokinetic phenomenon termed Field Amplified Sample Stacking (FASS) is found to be responsible for the inverse correlation between extra-cellular conductivity and the total delivery. This quantitative study validates our prediction tool, provides mechanistic interpretation to experimental trends, and furthermore makes a connection between the mesoscopic ASE model and macroscopic observables.

In examining the delivery efficiency of two-pulse electroporation, the correlation between Fluorescein-Dextran delivery and pulsing parameters is investigated quantitatively. As the main contribution of this task, the whole-cell level simulations capture the experimentally-observed existence of a threshold field strength above which the second pulse (LV) becomes effective in mediating molecular transport. Analysis of pore



dynamics reveals physical insights for this behavior, which results from a bifurcation point of equilibrium pore size with respect to the transmembrane potential. In addition to these findings, this model study provides useful predictions which can be verified with well-designed experiments.

In studying DNA delivery, the author focuses on investigating the "translocation theory", and has developed a 1D model in predicting the probability of successful translocation across a single electropore. This variable is supposed to be proportional to the total DNA delivery over the whole membrane. The main result of this work is a power-law correlation between the delivery and pulsing parameters. Such a correlation can be verified by experiments, which will in turn help check the validity of "translocation theory", and hence improves the current understanding about how DNA molecules enter the cell via electroporation.

In summary, this work has established connections between available theoretical tool and experimental observations. Overall, the tasks accomplished in this study contributes to improving the current understanding of the physical process involved in electroporation-mediated delivery, either for small-, moderate- or large-sized target molecules.

Besides electroporation research, the author has also performed a model study in vesicle/cell relaxation. The main result of this work is a small-deformation theory of vesicle relaxation. The author proves that, in the limit of infinitesimally small-deformation, the dynamics of vesicle relaxation is identical to that for a droplet. Physical insights are also revealed in differentiating the dominating mechanisms in small- and moderate-deformation, respectively. Preliminary results are shown in extracting membrane properties (bending rigidity) for different vesicle/cell types. This work contributes to the development of a reliable and promising theoretical tool of detecting mechanical properties of vesicles/biological cells.

## Appendix A

### Model formulation of electroporation-mediated delivery

#### A.1 The electrical problem

The overall model framework mostly follows that from our previous work [42]. The schematic of the problem is shown in Fig. A.1. The cell is modeled as a spherical space surrounded by a thin and rigid cell membrane. A 2D axissymmetric spherical coordinate system is adopted, with the direction of x axis aligned with the applied electric field. When the electric field is on, the cell membrane is partially permeabilized and the charged PI molecules can go through the permeabilized membrane into the cytoplasm. Since the charging relaxation time scale (in the order of nanoseconds) is very small compared to the process studied here (in the order of micro- to milli-seconds), the Ohmic equations are directly solved for the electric potentials inside and outside the cell, respectively:

$$\nabla \cdot \mathbf{j} = \nabla \cdot (\sigma_{i,e} \nabla \Phi_{i,e}) = 0, \quad (\text{A.1})$$

where  $\mathbf{j}$  denotes the Ohmic current vector,  $\sigma_{i,e}$  denote the intra- and extra-cellular conductivities, and  $\Phi_{i,e}$  denote the intra- and extra-cellular electric potentials, respectively. In this study,  $\sigma_{i,e}$  are both assumed to be constant, and their values are adopted from Sadik et al.'s experiments [72].

Equations (A.1) are coupled on the cell membrane by the electric current continuity condition across the membrane:

$$-\mathbf{n} \cdot \sigma_i \nabla \Phi_i = -\mathbf{n} \cdot \sigma_e \nabla \Phi_e = C_m \frac{\partial V_m}{\partial t} + j_p, \quad (\text{A.2})$$

where  $\mathbf{n}$  is the local unit vector normal to the membrane, and  $C_m$  is the membrane

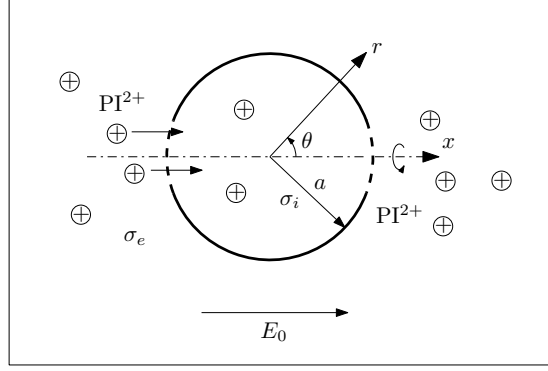


Figure A.1: A schematic of the problem.  $(r, \theta)$  denotes the spherical coordinate system.  $x$  is the axis of rotation, and is aligned with the direction of field application. The field strength is denoted by  $E_0$ . The intra- and extra-cellular conductivities are denoted by  $\sigma_i$  and  $\sigma_e$ , respectively.

capacitance.  $V_m$  is the transmembrane potential defined by the potential jump across the membrane  $(\Phi_i - \Phi_e)|_{r=R}$ . The last term  $j_p$  in Eq. (A.2) is the total local ionic current density through all the conductive pores generated by the electric field. The formula of  $j_p$  is adopted from Krassowska and Filev [35]:

$$j_p(t, \theta) = \sum_{j=1}^{K(t, \theta)} i_p(r_j(t, \theta), V_m) / \Delta A, \quad (\text{A.3})$$

where  $\Delta A$  is the area of local element,  $K$  is the total number of conductive pores, and  $i_p$  denotes the current through an individual pore with radius of  $r_j$  and local transmembrane potential of  $V_m$ .  $i_p$  is calculated by the formula:

$$i_p = \frac{2\pi r_j^2 \sigma_{eff} V_m}{\pi r_j + 2h}, \quad (\text{A.4})$$

where  $\sigma_{eff} = (\sigma_e - \sigma_i) / \ln(\sigma_e / \sigma_i)$  is an effective pore conductivity and  $h$  is the membrane thickness. The detailed derivation of Eq. (A.4) can be found in [40].

## A.2 Membrane permeabilization

The ASE model derived by Krassowska and Filev [35] is adopted to solve for the nucleation of electropores and evolution of radius for each individual pore:

$$\frac{dN}{dt} = \alpha e^{(V_m/V_{ep})^2} \left( 1 - \frac{N}{N_0 e^{q(V_m/V_{ep})^2}} \right), \quad (\text{A.5})$$

$$\frac{dr_j}{dt} = U(r_j, V_m), \quad j = 1, 2, \dots, K(t, \theta). \quad (\text{A.6})$$

Here  $N$  is the local pore number density,  $U$  denotes the advective velocity of pore evolution in size and  $\alpha$ ,  $V_{ep}$ ,  $N_0$ ,  $q$  are model constants. In this model, each pore is generated at an initial radius of 0.51 nm, and the rate of nucleation is governed by Eq. (A.5). The dynamics of size evolution for each pore are then captured by Eq. (A.6), which requires the total energy of the lipid membrane at its minimum. After the electric field turns off, the electropores will reseal, which effect is also captured by the current permealization model. Further details of the model including the values of model parameters adopted can be found in [35].

### A.3 Species transport

As shown in Fig. A.1, the free PI ions (denoted by  $\text{PI}^{2+}$ ) are delivered into the cytoplasm after the cell membrane is permeabilized. The delivered  $\text{PI}^{2+}$  will bind to the DNA/RNA sites (denoted by B) in the cytoplasm or the nucleus and become bound PI (denoted by PIB) which is fluorescent such as to be experimentally observed. To fully take into such a binding effect into account, three specific species, namely,  $\text{PI}^{2+}$ , B and PIB are considered in the simulations. It is assumed that before the electric pulse is applied, the binding sites are only uniformly distributed in the cytoplasm at an initial molar concentration of  $[\text{B}]_{i,o}$ , and the free PI ions are only uniformly distributed in the extra-cellular space at an initial molar concentration of  $[\text{PI}^{2+}]_{e,o}$ . Here the subscript  $i$  indicates an intra-cellular value,  $e$  indicates an extra-cellular value and  $o$  indicates an initial value. The binding sites are assumed to immobile, and the following chemical reaction will take place after free PI ions are accessed into the cell:



Here  $k_+$  and  $k_-$  are the association and dissociation rate constants, respectively. The bound PI molecules are also assumed to immobile.

A generalized Nernst-Planck system is adopted to solve for the ionic transport of  $\text{PI}^{2+}$ , B and PIB. The effect of chemical reaction manifests itself as the source and sink terms in the transport equations. As both B and PIB are immobile, their transport equations are simply derived from the evolution of local species concentration due to chemical reaction.

The equations for ionic transport are:

$$\frac{\partial[\text{PI}^{2+}]}{\partial t} = \nabla \cdot (\omega F z [\text{PI}^{2+}] \nabla \Phi) + \nabla \cdot (D \nabla [\text{PI}^{2+}]) - k_+ [\text{B}] [\text{PI}^{2+}] + k_- [\text{PIB}], \quad (\text{A.8})$$

$$\frac{\partial[\text{B}]}{\partial t} = -k_+ [\text{B}] [\text{PI}^{2+}] + k_- [\text{PIB}], \quad (\text{A.9})$$

$$\frac{\partial[\text{PIB}]}{\partial t} = k_+ [\text{B}] [\text{PI}^{2+}] - k_- [\text{PIB}], \quad (\text{A.10})$$

where  $[\text{PI}^{2+}]$ ,  $[\text{B}]$ ,  $[\text{PIB}]$  denote the molar concentrations for each species, respectively.  $F$  is the Faraday constant,  $\omega$ ,  $z$ ,  $D$  denote the mechanical mobility, the valence number and the diffusivity of  $\text{PI}^{2+}$ , respectively. Eqs. (A.8)-(A.10) are solved in both the intra- and extra-cellular spaces. They are coupled on the membrane by the continuity of molar flux density for  $\text{PI}^{2+}$ :

$$F_{i,e} = F_m, \quad (\text{A.11})$$

where  $F_{i,e}$  are the species flux densities from the intra- and extra-cellular space, respectively, and  $F_m$  is the flux density across the cell membrane.  $F_{i,e}$  and  $F_m$  are calculated by the formula:

$$F_{i,e} \equiv -\mathbf{n} \cdot (\omega F z [\text{PI}^{2+}] \nabla \Phi + D \nabla [\text{PI}^{2+}])_{i,e}, \quad (\text{A.12})$$

$$F_m \equiv \rho_p \frac{D(Pe + \ln \gamma)}{h} \frac{\gamma - 1}{\ln \gamma} \frac{([PI^{2+}]_e - [PI^{2+}]_i \exp(Pe))}{(1 - \gamma \exp(Pe))}. \quad (A.13)$$

Here the Peclet Number is defined as  $Pe \equiv \omega F z V_m / D$ .  $\gamma = \sigma_i / \sigma_e$  is the intra-to-extra-cellular conductivity ratio. The pore area density (PAD)  $\rho_p$  indicates the fractional area occupied by the conductive pores, which is given by the following pore statistics:

$$\rho_p(t, \theta) = \sum_{j=1}^{K(t, \theta)} \pi r_j^2 / \Delta A. \quad (A.14)$$

$\rho_p$  is frequently used as a measurement of the membrane permeabilization level. In deriving Eqs. (A.11)-(A.13), it is assumed that the sum of electrophoretic and diffusive flux within each pore is constant along its axis.

#### A.4 Numerical implementation

The system of Eqs. (A.1)-(A.14) is numerically solved with a finite-volume, alternative direction implicit (ADI) scheme. The problem is solved under a 2D axisymmetric spherical coordinate system. Initially, the membrane is intact with no electropores and the electric potentials inside and outside the cell are uniformly  $V_{rest}$  and zero, respectively:

$$N(t = 0, \theta) = 0, \quad \Phi_i(t = 0) = V_{rest}, \quad \Phi_e(t = 0) = 0. \quad (A.15)$$

As introduced in Section A.3, the initial extra-cellular concentration of  $PI^{2+}$  and intra-cellular concentration of B are both assumed to be uniformly distributed.

The boundary of numerical domain is taken to be far away from the cell (at  $r = 20a$ ), where the electric field is approximated to be the same as the applied one, and the concentration of  $PI^{2+}$  is fixed at its initial value:

$$\Phi_e(t, r = 20a, \theta) = -E_0 r \cos(\theta), \quad [PI^{2+}](t, r = 20a, \theta) = [PI^{2+}]_{e,o}. \quad (A.16)$$

Here  $E_0$  is the strength of the applied electric field.

## Appendix B

### Supplements for Chapter 4

A main difference between the model in Chapter 4 and previous ones [50, 82] is that a specific value for  $k_0$ , which we determine from  $D_0$ , the chain diffusivity, is required. The latter can be obtained from experimental measurements. The relationship between  $k_0$  and  $D_0$  can be derived by considering the Fokker-Planck equation in the natural coordinate, namely, the center of mass of the entire chain,  $x$ :

$$\frac{\partial P(x, t)}{\partial t} = \frac{\partial}{\partial x} \left[ \frac{D_0}{k_B T} P(x, t) \frac{\partial f(x, t)}{\partial x} + D_0 \frac{\partial}{\partial x} P(x, t) \right]. \quad (\text{B.1})$$

Comparing Eq. (B.1) with Eq. (4.1), and considering  $x = mL$ ,  $k_0 = D_0/L^2$  is obtained. Here, the characteristic length  $L$  is taken to be  $2R_g/N$  (Fig. B.1), where  $R_g$  is the radius of gyration. In other words, the translocation of the complete  $N$  segments is equivalent to a distance of  $2R_g$  traveled by the center of mass. Further considering that  $R_g = 0.459l_k N^{0.6}$ , which is derived for a polymer chain with one end pinned on a rigid wall [11], Eq. (4.2) in the proper text can be obtained.

The bulk diffusivity of an  $N$ -segment DNA chain is found by the measurements of Dauty *et al.* [9],

$$D_{bulk} = \frac{1.344 \times 10^{-11}}{N^{0.68}} \text{ m}^2/\text{s}. \quad (\text{B.2})$$

For the current model, a modified formula based on Eq. (B.2) is used,

$$D_0 = \alpha \beta D_{bulk}. \quad (\text{B.3})$$

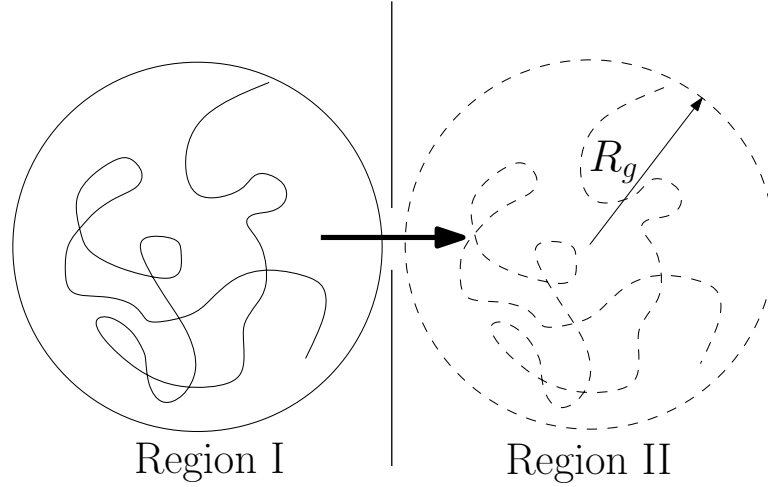


Figure B.1: Upon the completion of translocation, the center of mass translates by  $2R_g$ , where  $R_g$  is the radius of gyration.

The factor  $\alpha$  arises from a reduction due to the crowdedness of the cytoplasm. Extrapolating from the measurements by Dauty *et al.* (see Fig. 4B therein),  $\alpha = 0.017$  is used for a chain length of 4.7 kbp, and  $\alpha = 0.01$  is used for a chain length of 7.2 kbp.

The factor  $\beta$  is the reduction effect due to the fact that the polymer chain is in the vicinity of a rigid wall. According to the measurements by Kihm *et al.* for solid nanoparticles [30], this factor typically ranges from 0 to 0.6 depending on the distance from the wall. Due to the lack of data for near-wall DNA particles,  $\beta$  is simply used as a fitting parameter to generate the best comparison with data on DNA translation through synthesized nanopores [80]. From Fig. B.2,  $\beta = 0.322$  is obtained to achieve the best matching between our theoretical prediction and the measurements. Note to generate this comparison,  $\alpha = 1$  is used because no cells are involved.

As a remark, Eq. (B.3) gives a constant  $D_0$  given a constant size of DNA. A more accurate model can be derived where  $D_0$  is a function of the translocation coordinate,  $m$  [82]. However, it is found that no appreciable difference between the results following this approach and simply using Eq. (B.3) above. (The comparison is not shown here for brevity.) The agreement results from the fact that the effective diffusivity of the DNA chain is dominantly controlled by its much reduced value in the cytoplasm. In this work, Eq. (B.3) is therefore used as an approximation to the more complete diffusivity



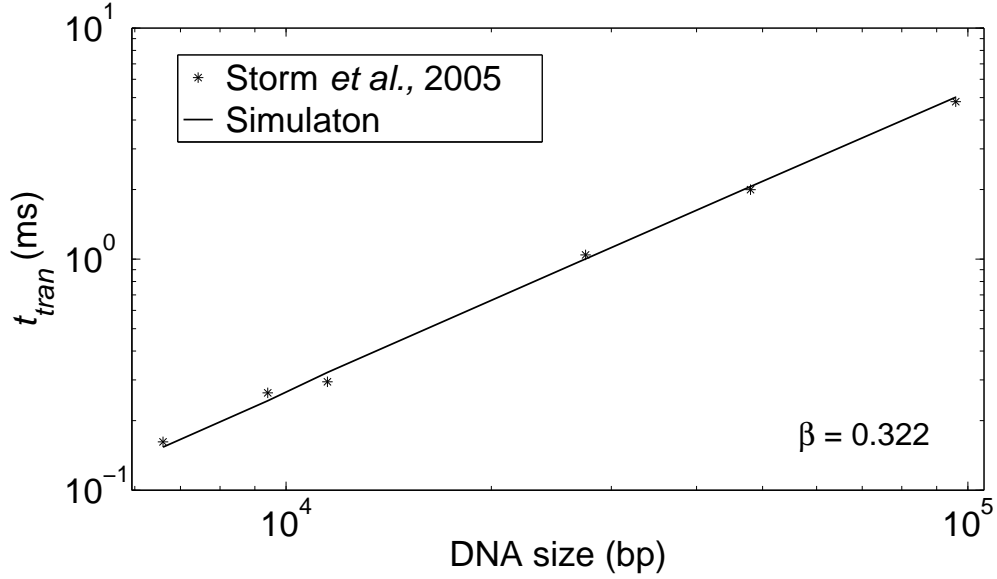


Figure B.2: Simulated results with  $\beta = 0.322$ , in comparison with the experimental data from Storm *et al.* [80]. The average translocation time  $t_{tran}$  is plotted as a function of DNA size. The transmembrane potential is  $V_m = 0.12$  V. The average translocation time is defined as the most probable time required for the DNA molecule to complete its translocation.

model.

The effective charge per DNA segment,  $\tilde{z}_s$ , is given by the formula,

$$\tilde{z}_s = 0.5 \times \frac{L}{l_{bp}} = 135N^{-0.4}. \quad (\text{B.4})$$

The factor of 0.5 is obtained from the experiments by Keyser *et al.* [29], which suggests that the effective charge of a DNA base pair (2 electrons) is reduced by 75% within a pore. This reduction ratio corroborates with the theoretical prediction by Ghosal [20], which attributes the effects to viscous drags within the pore. Again, although these results are generated for solid-state nanopores, they are employed in this work due to the lack of measurements for electropores.

## Appendix C

### Supplements for Chapter 5

The solution of intra- and extra-vesicular velocities can be derived from Eq. (5.2) and Eqs. (5.17)-(5.18). The results are:

$$\begin{cases} u_r^i = -(1 - 3 \cos^2 \theta)(C \frac{r}{a} + D \frac{r^3}{a^3}) \\ u_r^e = -(1 - 3 \cos^2 \theta)(A \frac{a^4}{r^4} + B \frac{a^2}{r^2}) \\ u_\theta^i = -\sin \theta \cos \theta (3C \frac{r}{a} + 5D \frac{r^3}{a^3}) \\ u_\theta^e = \sin \theta \cos \theta \cdot 2A \frac{a^4}{r^4} \end{cases} . \quad (\text{C.1})$$

The solution of pressure can then be derived from Eq. (5.3):

$$\begin{cases} p_i = -\mu_i \frac{7Dr^2}{a^3} (1 - 3 \cos^2 \theta) \\ p_e = -\mu_e \frac{2Ba^2}{r^3} (1 - 3 \cos^2 \theta) \end{cases} . \quad (\text{C.2})$$

In axisymmetric spherical coordinate system, The stress components are correlated with velocity and pressure field by:

$$\begin{cases} T_{rr} = -p + 2\mu \frac{\partial u_r}{\partial r} \\ T_{r\theta} = \mu [r \frac{\partial}{\partial r} (\frac{u_\theta}{r}) + \frac{1}{r} \frac{\partial u_r}{\partial \theta}] \end{cases} . \quad (\text{C.3})$$

With the solution in Eq. (C.1) and (C.2), the expressions of stress components are:

$$\begin{cases} T_{rr}^i = \mu_i(1 - 3\cos^2\theta)(\frac{Dr^2}{a^3} - \frac{2C}{a}) \\ T_{rr}^e = \mu_e(1 - 3\cos^2\theta)(\frac{6Ba^2}{r^3} + \frac{8Aa^4}{r^5}) \\ T_{r\theta}^i = -\mu_i \sin\theta \cos\theta \frac{6Ca^2 + 16Dr^2}{a^3} \\ T_{r\theta}^e = -\mu_e \sin\theta \cos\theta \frac{16Aa^4 + 6Ba^2r^2}{r^5} \end{cases} . \quad (C.4)$$

The normal membrane stress arising from membrane tension  $f_n^{mem} = 2\Gamma H$ . Here  $H = \frac{1}{2}(\frac{1}{R_1} + \frac{1}{R_2})$  where  $1/R_1$  and  $1/R_2$  are principal curvatures at a given point on the surface of a spheroid. In deriving the solution, the leading order expansions of  $1/R_1$  and  $1/R_2$  are used:

$$\begin{cases} \frac{1}{R_1} = \frac{1}{a}[1 + (3\cos^2\theta - \frac{5}{3})(e-1) + O(e-1)^2] \\ \frac{1}{R_2} = \frac{1}{a}[1 + (\cos^2\theta + \frac{1}{3})(e-1) + O(e-1)^2] \end{cases} . \quad (C.5)$$

## Bibliography

- [1] F. André and L. M. Mir. DNA electrotransfer: its principles and an updated review of its therapeutic applications. *Gene Ther.*, 11:S33–S42, 2004.
- [2] F. M. André, J. Gehl, G. Sersa, V. Prémat, P. Hojman, J. Eriksen, M. Golzio, M. Cemazar, N. Pavselj, M.-P. Rols, D. Miklavčič, E. Neumann, J. Teissié, and L. M. Mir. Efficiency of high- and low-voltage pulse combinations for gene electrotransfer in muscle, liver, tumor, and skin. *Hum. Gene Ther.*, 19:1261–1271, 2008.
- [3] A. Barnett and J. C. Weaver. Electroporation: a unified, quantitative theory of reversible electrical breakdown and mechanical rupture in artificial planar bilayer membranes. *Bioelectrochem. Bioenerg.*, 25:163–182, 1991.
- [4] M. F. Bureau, J. Gehl, V. Deleuze, L. M. Mir, and D. Scherman. Importance of association between permeabilization and electrophoretic forces for intramuscular DNA electrotransfer. *Biochim. Biophys. Acta*, 1474:353–359, 2000.
- [5] P. J. Canatella, J. F. Karr, J. A. Petros, and M. R. Prausnitz. Quantitative study of electroporation-mediated molecular uptake and cell viability. *Biophys. J.*, 80(2):755–764, 2001.
- [6] D. C. Chang and T. S. Reese. Changes in membrane structure induced by electroporation as revealed by rapid-freezing electron microscopy. *Biophys. J.*, 58:1–12, 1990.
- [7] C. Chen, S. W. Smye, M. P. Robinson, and J. A. Evans. Membrane electroporation theories: a review. *Med Biol Eng Comput*, 44:5–14, 2006.

- [8] M. Costa, M. Dottori, K. Sourris, P. Jamshidi, T. Hatzistavrou, R. Davis, L. Az-zola, S. Jackson, S. M. Lim, M. Pera, A. G. Elefanty, and E. G. Stanley. A method for genetic modification of human embryonic stem cells using electroporation. *Nat. Protoc.*, 2:792–796, 2007.
- [9] E. Dauty and A. S. Verkman. Actin cytoskeleton as the principal determinant of size-dependent DNA mobility in cytoplasm. *J. Biol. Chem.*, 280(9):7823–7828, 2005.
- [10] C. S. Djuzenova, U. Zimmermann, H. Frank, V. L. Sukhorukov, E. Richter, and G. Fuhr. Effect of medium conductivity and composition on the uptake of propidium iodide into electroporabilized myeloma cells. *Biochim. Biophys. Acta*, 1284:143–152, 1996.
- [11] E. Eisenriegler, K. Kremer, and K. Binder. Adsorption of polymer chains at surfaces: Scaling and monte carlo analyses. *J. Chem. Phys.*, 77(12):6296–6319, 1982.
- [12] J.-M. Escoffre, T. Portet, C. Favard, J. Teissié, D. S. Dean, and M.-P. Rols. Electromediated formation of DNA complexes with cell membranes and its consequences for gene delivery. *Biochim. Biophys. Acta*, 1808:1538–1543, 2011.
- [13] J.-M. Escoffre, T. Portet, L. Wasungu, J. Teissié, D. Dean, and M.-P. Rols. What is (still not) known of the mechanism by which electroporation mediates gene transfer and expression in cells and tissues. *Mol Biotechnol*, 41:286–295, 2009.
- [14] C. Faurie, E. Phez, M. Golzio, C. Vossen, J.-C. Lesbordes, C. Delteil, J. Teissié, and M.-P. Rols. Effect of electric field vectoriality on electrically mediated gene delivery in mammalian cells. *Biochim. Biophys. Acta*, 1665:92–100, 2004.
- [15] C. Faurie, M. Reberšek, M. Golzio, M. Kandušer, J.-M. Escoffre, M. Pavlin, J. Teissié, D. Miklavčič, and M.-P. Rols. Electro-mediated gene transfer and expression are controlled by the life-time of DNA/membrane complex formation. *The Journal of Gene Medicine*, 12:117–125, 2010.

- [16] B. Flickinger, T. Berghöfer, P. Hohenberger, C. Eing, and W. Frey. Transmembrane potential measurements on plant cells using the voltage-sensitive dye ANNINE-6. *Protoplasma*, 247:3–12, 2010.
- [17] S. A. Freeman, M. A. Wang, and J. C. Weaver. Theory of electroporation of planar bilayer membranes: Predictions of the aqueous area, change in capacitance, and pore-pore separation. *Biophys. J.*, 67:42–56, 1994.
- [18] B. Gabriel and J. Teissié. Control by electrical parameters of short- and long-term cell death resulting from electroporation of chinese hamster ovary cells. *Biochim. Biophys. Acta*, 1266(2):171–178, 1995.
- [19] J. Gehl. Electroporation: theory and methods, perspectives for drug delivery, gene therapy and research. *Acta Physiol. Scand.*, 177(4):437–447, 2003.
- [20] S. Ghosal. Electrokinetic-flow-induced viscous drag on a tethered DNA inside a nanopore. *Phys. Rev. E*, 76:061916, 2007.
- [21] M. Golzio, M.-P. Mora, C. Raynaud, C. Delteil, J. Teissié, and M.-P. Rols. Control by osmotic pressure of voltage-induced permeabilization and gene transfer in mammalian cells. *Biophys. J.*, 74:3015–3022, 1998.
- [22] M. Golzio, J. Teissié, and M.-P. Rols. Direct visualization at the single-cell level of electrically mediated gene delivery. *Proc. Nat. Acad. Sci. U.S.A.*, 99(3):1292–1297, 2002.
- [23] J. Guck, S. Schinkinger, B. Lincoln, F. Wottawah, S. Ebert, M. Romeyke, D. Lenz, H. M. Erickson, R. Ananthakrishnan, D. Mitchell, J. Käs, S. Ulvick, and C. Bilby. Optical deformability as an inherent cell marker for testing malignant transformation and metastatic competence. *Biophys. J.*, 88(5):3689–3698, 2005.
- [24] S. Guido and M. Villone. Measurement of interfacial tension by drop retraction analysis. *J. Colloid Interface Sci.*, 209:247–250, 1999.

- [25] H. He, D. C. Chang, and Y.-K. Lee. Nonlinear current response of micro electroporation and resealing dynamics for human cancer cells. *Bioelectrochemistry*, 72(2):161–168, 2008.
- [26] W. Helfrich and R.-M. Servuss. Undulations, steric interaction and cohesion of fluid membranes. *Il Nuovo Cimento*, 3D:137–151, 1984.
- [27] L. C. Heller and R. Heller. In vivo electroporation for gene therapy. *HUMAN GENE THERAPY*, 17:890–897, 2006.
- [28] M. Kandušer, D. Miklavčič, and M. Pavlin. Mechanisms involved in gene electro-transfer using high- and low-voltage pulses - an in vitro study. *Bioelectrochemistry*, 74:265–271, 2009.
- [29] U. F. Keyser, B. N. Koeleman, S. van Dorp, D. Krapf, R. M. M. Smeets, S. G. Lemay, N. H. Dekker, and C. Dekker. Direct force measurements on DNA in a solid-state nanopore. *Nat. Phys.*, 2:473–477, 2006.
- [30] K. D. Kihm, A. Banerjee, C. K. Choi, and T. Takagi. Near-wall hindered brownian diffusion of nanoparticles examined by three-dimensional ratiometric total internal reflection fluorescence microscopy (3-D R-TIRFM). *Exp. Fluids*, 37:811–824, 2004.
- [31] Jr. K. Kinoshita, I. Ashikawa, N. Saita, H. Yoshimura, H. Itoh, K. Nagayama, and A. Ikegami. Electroporation of cell membrane visualized under a pulsed-laser fluorescence microscope. *Biophys. J.*, 53:1015–1019, 1988.
- [32] V. A. Klenchin, S. I. Sukharev, S. M. Serov, L. V. Chernomordik, and Yu. A. Chizmadzhev. Electrically induced DNA uptake by cells is a fast process involving dna electrophoresis. *Biophys. J.*, 60:804–811, 1991.
- [33] T. Kotnik, G. Pucihar, M. Reberšek, D. Miklavčič, and L. M. Mir. Role of pulse shape in cell membrane electroporation. *Biochim. Biophys. Acta*, 1614:193–200, 2003.

- [34] P. Kramar, L. Delemotte, A. M. Lebar, M. Kotulska, M. Tarek, and D. Miklavčič. Molecular-level characterization of lipid membrane electroporation using linearly rising current. *Journal of Membrane Biology*, 245(10):651–659, 2012.
- [35] W. Krassowska and P. D. Filev. Modeling electroporation in a single cell. *Biophys. J.*, 92(2):404–417, 2007.
- [36] M. Kummrow and W. Helfrich. Deformation of giant lipid vesicles by electric fields. *Phys. Rev. A*, 44:8356, 1991.
- [37] H. Leontiadou, A. E. Mark, and S. J. Marrink. Molecular dynamics simulations of hydrophilic pores in lipid bilayers. *Biophys. J.*, 86:2156–2164, 2004.
- [38] Z. A. Levine and P. T. Vernier. Life cycle of an electropore: Field-dependent and field-independent steps in pore creation and annihilation. *J Membrane Biol*, 236:27–36, 2010.
- [39] J. Li, M. Gershow, D. Stein, E. Brandin, and J. A. Golovchenko. DNA molecules and configurations in a solidstate nanopore microscope. *Nat. Mater.*, 2:611–615, 2003.
- [40] J. Li and H. Lin. The current-voltage relation for electropores with conductivity gradients. *Biomicrofluidics*, 4:013206, 2010.
- [41] J. Li and H. Lin. Numerical simulation of molecular uptake via electroporation. *Bioelectrochemistry*, 82:10–21, 2011.
- [42] J. Li, W. Tan, M. Yu, and H. Lin. The effect of extracellular conductivity on electroporation mediated molecular delivery. *BBA Biomembranes*, 1828(2):461–470, 2013.
- [43] R. Lin, D. C. Chang, and Y.-K. Lee. Single-cell electroendocytosis on a micro chip using in situ fluorescence microscopy. *Biomed. Microdevices*, 13:1063–1073, 2011.



- [44] F. Liu, S. Heston, L. M. Shollenberger, B. Sun, M. Mickle, M. Lovell, and L. Huang. Mechanism of in vivo DNA transport into cells by electroporation: electrophoresis across the plasma membrane may not be involved. *Journal of Gene Medicine*, 8:353–361, 2006.
- [45] D. Miklavčič and L. Towhidi. Numerical study of the electroporation pulse shape effect on molecular uptake of biological cells. *Radiol Oncol*, 44(1):34–41, 2010.
- [46] L. M. Mir. Therapeutic perspectives of in vivo cell electroporabilization. *Bioelectrochemistry*, 53:1–10, 2000.
- [47] L. M. Mir, M. F. Bureau, J. Gehl, R. Rangara, D. Rouyi, J.-M. Caillaud, P. Delaere, D. Branelleci, B. Schwartz, and D. Scherman. High-efficiency gene transfer into skeletal muscle mediated by electric pulses. *Proc. Natl. Acad. Sci.*, 96:4262–4267, 1999.
- [48] L. M. Mir, S. Orlowski, J. Belehradek Jr., J. Teissié, M.-P. Rols, G. Serša, D. Miklavčič, R. Gilbert, and R. Heller. Biomedical applications of electric pulses with special emphasis on antitumor electrochemotherapy. *Bioelectrochem. Bioenerg.*, 38:203–207, 1995.
- [49] K. J. Müller, V. L. Sukhorukov, and U. Zimmermann. Reversible electroporabilization of mammalian cells by high-intensity, ultra-short pulses of submicrosecond duration. *J. Membrane Biol.*, 184:161–170, 2001.
- [50] M. Muthukumar. Polymer translocation through a hole. *J. Chem. Phys.*, 111(22):10371–10374, 1999.
- [51] M. Muthukumar. Theory of capture rate in polymer translocation. *J. Chem. Phys.*, 132:195101, 2010.
- [52] T. B. Napotnik, Y.-H. Wu, M. A. Gundersen, D. Miklavčič, and P. T. Vernier. Nanosecond electric pulses cause mitochondrial membrane permeabilization in jurkat cells. *Bioelectromagnetics*, 33(3):257–264, 2012.

- [53] R. E. Neal II and R. V. Davalos. The feasibility of irreversible electroporation for the treatment of breast cancer and other heterogeneous systems. *Ann. Biomed. Eng.*, 37:2615–2625, 2009.
- [54] J. C. Neu and W. Krassowska. Asymptotic model of electroporation. *Phys. Rev. E*, 59(3):3471–3482, 1999.
- [55] J. C. Neu and W. Krassowska. Modeling postshock evolution of large electropores. *Phys. Rev. E*, 67:021915, 2003.
- [56] E. Neumann, M. Schaefer-Ridder, Y. Wang, and P. H. Hofschneider. Gene transfer into mouse lyoma cells by electroporation in high electric fields. *The EMBO Journal*, 1(7):841–845, 1982.
- [57] E. Neumann, A. E. Sowers, and C. A. Jordan, editors. *Electroporation and Electrofusion in cell Biology*. Plenum Press, 1989.
- [58] R. Nuccitelli, U. Pliquett, X. Chen, W. Ford, R. J. Swanson, S. J. Beebe, J. F. Kolb, and K. H. Schoenbach. Nanosecond pulsed electric fields cause melanomas to self-destruct. *Biochem. Biophys. Res. Commun.*, 343:351–360, 2006.
- [59] M. Pavlin, K. Flisar, and M. Kandušer. The role of electrophoresis in gene electrotransfer. *J. Membrane Biol.*, 236:75–79, 2010.
- [60] M. Pavlin, M. Kandušer, G. Pucihar, and D. Miklavčič. The role of electrically stimulated endocytosis in gene electrotransfer. *IFMBE Proceedings*, 29:679–682, 2010.
- [61] N. Pavšelj and V. Pr  at. DNA electrotransfer into the skin using a combination of one high- and one low-voltage pulse. *J. Controlled Release*, 106:407–415, 2005.
- [62] E. Phez, C. Faurie, M. Golzio, J. Teissi  , and M.-P. Rols. New insights in the visualization of membrane permeabilization and DNA/membrane interaction of cells submitted to electric pulses. *Biochim. Biophys. Acta*, 1724:248–254, 2005.

- [63] M. R. Prausnitz, J. D. Corbett, J. A. Gimm, D. E. Golan, R. Langer, and J. C. Weaver. Millisecond measurement of transport during and after an electroporation pulse. *Biophys. J.*, 68(5):1864–1870, 1995.
- [64] G. Pucihar, T. Kotnik, D. Miklavčič, and J. Teissié. Kinetics of transmembrane transport of small molecules into electroporabilized cells. *Biophys. J.*, 95:2837–2848, 2008.
- [65] K. A. Riske and R. Dimova. Electro-deformation and poration of giant vesicles viewed with high temporal resolution. *Biophys. J.*, 88:1143, 2005.
- [66] K. A. Riske and R. Dimova. Personal communication. 2013.
- [67] M.-P. Rols. Electroporabilization, a physical method for the delivery of therapeutic molecules into cells. *Biochim. Biophys. Acta*, 1758:423–428, 2006.
- [68] M.-P. Rols and J. Teissié. Electroporabilization of mammalian cells to macromolecules: Control by pulse duration. *Biophys. J.*, 75:1415–1423, 1998.
- [69] C. Rosazza, E. Phez, J.-M. Escoffre, L. Cézanne, A. Zumbusch, and M.-P. Rols. Cholesterol implications in plasmid DNA electrotransfer: Evidence for the involvement of endocytotic pathways. *Int. J. Pharm.*, 423:134–143, 2012.
- [70] B. Rubinsky. Irreversible electroporation in medicine. *Technol. Cancer Res. Treat.*, 6(4):255–259, 2007.
- [71] M. M. Sadik, J. Li, J. W. Shan, D. I. Shreiber, and H. Lin. Vesicle deformation and poration under strong dc electric fields. *Phy. Rev. E.*, 83:066316, 2011.
- [72] M. M. Sadik, J. Li, J. W. Shan, D. I. Shreiber, and H. Lin. Quantification of propidium iodide delivery using milisecond electric pulses: Experiments. *BBA Biomembranes*, 1828:1322–1328, 2013.
- [73] M. M. Sadik, M. Yu, J. W. Shan, D. I. Shreiber, and H. Lin. Scaling relationship and optimization of double-pulse electroporation. *Biophys. J.*, 106:801–812, 2014.

- [74] K. H. Schoenbach, R. P. Joshi, J. F. Kolb, N. Chen, M. Stacey, P. F. Blackmore, E. S. Buescher, and S. J. Beebe. Ultrashort electrical pulses open a new gateway into biological cells. *Proc. IEEE*, 92(7):1122–1136, 2004.
- [75] K. H. Schoenbach, R. P. Joshi, R. H. Stark, F. C. Dobbs, and S. J. Beebe. Bacterial decontamination of liquids with pulsed electric fields. *IEEE Trans. Dielectr. Electr. Insul.*, 7(5):637, 2000.
- [76] E. Slonkina and A. B. Kolomeisky. Polymer translocation through a long nanopore. *J. Chem. Phys.*, 118(15):7112–7118, 2003.
- [77] K. C. Smith, J. C. Neu, and W. Krassowska. Model of creation and evolution of stable electropores for DNA delivery. *Biophys. J.*, 86:2813–2826, 2004.
- [78] K. C. Smith and J. C. Weaver. Transmembrane molecular transport during versus after extremely large, nanosecond electric pulses. *Biochem. Biophys. Res. Commun.*, 412:8–12, 2011.
- [79] M. Spassova, I. Tsoneva, A. G. Petrov, J. I. Petkova, and E. Neumann. Dip patch clamp currents suggest electrodiffusive transport of the polyelectrolyte dna through lipid bilayers. *Biophys. Chem.*, 52(3):267–274, 1994.
- [80] A. J. Storm, C. Storm, J. Chen, H. Zandbergen, J.-F. Joanny, and C. Dekker. Fast DNA translocation through a solid-state nanopore. *Nano Lett.*, 5(7):1193–1197, 2005.
- [81] S. I. Sukharev, V. A. Klenchin, S. M. Serov, L. V. Chernomordik, and Yu. A. Chizmadzhev. Electroporation and electrophoretic DNA transfer into cells: the effect of DNA interaction with electropores. *Biophys. J.*, 63:1320–1327, 1992.
- [82] W. Sung and P. J. Park. Polymer translocation through a pore in a membrane. *Phys. Rev. Lett.*, 77(4):783–786, 1996.
- [83] S. Suresh. Biomechanics and biophysics of cancer cells. *Acta Biomater.*, 3:413, 2007.

- [84] D. O. H. Suzuki, A. Ramos, M. C. M. Ribeiro, L. H. Cazarolli, F. R. M. B. Silva, L. D. Leite, and J. L. B. Marques. Theoretical and experimental analysis of electroporated membrane conductance in cell suspension. *IEEE Trans. Biomed. Eng.*, 58(12):3310–3318, 2011.
- [85] M. Tarek. Membrane electroporation: A molecular dynamics simulation. *Biophys. J.*, 88(6):4045–4053, 2005.
- [86] J. Teissié, J.-M. Escoffre, A. Paganin, S. Chabot, E. Bellard, L. Wasungu, M.-P. Rols, and M. Golzio. Drug delivery by electropulsation: Recent developments in oncology. *Int. J. Pharm.*, 423(1):3–6, 2012.
- [87] Y. Teng and C. Xiong. Personal communication. 2013.
- [88] H. T. Tien and A. Ottova. The bilayer lipid membrane (BLM) under electrical fields. *IEEE Trans. Dielectr. Electr. Insul.*, 10(5):717–727, 2003.
- [89] A. Van Driessche, P. Ponsaerts, D. R. Van Bockstaele, V. F. I. Van Tendeloo, and Z. N. Bernema. Messenger RNA electroporation: an efficient tool in immunotherapy and stem cell research. *Folia Histochemica et Cytobiologica*, 43(4):213–216, 2005.
- [90] J. L. Vásquez, J. Gehl, and G. G. Hermann. Electroporation enhances mitomycin C cytotoxicity on T24 bladder cancer cell line: A potential improvement of intravesical chemotherapy in bladder cancer. *Bioelectrochemistry*, 88:127–133, 2012.
- [91] J. L. Viovy. Electrophoresis of DNA and other polyelectrolytes: Physical mechanisms. *Rev. Mod. Phys.*, 72(3):813–871, 2000.
- [92] P. M. Vlahovska, R. S. Gracià, S. Aranda-Espinoza, and R. Dimova. Electrohydrodynamic model of vesicle deformation in alternating electric fields. *Biophys. J.*, 96(12):4789–4803, 2009.
- [93] S. Šatkauskas, F. André, M. F. Bureau, D. Scherman, D. Miklavčič, and L. M.

- Mir. Electrophoretic component of electric pulses determines the efficacy of in vivo DNA electrotransfer. *Hum. Gene Ther.*, 16:1194–1201, 2005.
- [94] S. Šatkauskas, M. F. Bureau, M. Puc, A. Mahfoudi, D. Scherman, D. Miklavčič, and L. M. Mir. Mechanisms of in vivo DNA electrotransfer: Respective contributions of cell electroporabilization and DNA electrophoresis. *Molecular Therapy*, 5(2):133–140, 2002.
- [95] J. C. Weaver and Yu. A. Chizmadzhev. Theory of electroporation: A review. *Bioelectrochem. Bioenerg.*, 41:135–160, 1996.
- [96] L. H. Wegner, B. Flickinger, C. Eing, T. Berghöfer, P. Hohenberger, W. Frey, and P. Nick. A patch clamp study on the electro-permeabilization of higher plant cells: Supra-physiological voltages induce a high-conductance, K<sup>+</sup> selective state of the plasma membrane. *Biochim. Biophys. Acta*, 1808:1728–1736, 2011.
- [97] C. Wilhelm, M. Winterhalter, U. Zimmermann, and R. Benz. Kinetics of pore size during irreversible electrical breakdown of lipid bilayer membranes. *Biophys. J.*, 64:121–128, 1993.
- [98] H. Wolf, M.-P. Rols, E. Boldt, E. Neumann, and J. Teissié. Control by pulse parameters of electric field-mediated gene transfer in mammalian cells. *Biophys. J.*, 66:524–531, 1994.
- [99] M. Wu and F. Yuan. Membrane binding of plasmid DNA and endocytic pathways are involved in electrotransfection of mammalian cells. *PLoS ONE*, 6(6):e20923, 2011.
- [100] M. Yu and H. Lin. Quantification of propidium iodide delivery with milisecond electric pulses: A model study, submitted.
- [101] M. Yu, W. Tan, and H. Lin. A stochastic model for DNA translocation through an electropore. *BBA Biomembranes*, 1818(11):2494–2501, 2012.
- [102] G. Zhang, M. Long, Z.-Z. Wu, and W.-Q. Yu. Mechanical properties of hepatocellular carcinoma cells. *World J Gastroenterol.*, 8(2):243–246, 2002.

- [103] J. Zhang, J. D. Zahn, and H. Lin. Transient solution for droplet deformation under electric fields. *Phys. Rev. E*, 87:043008, 2013.
- [104] J. Zhang, J. D. Zahn, W. Tan, and H. Lin. A transient solution for vesicle electrodeformation and relaxation. *Phys. Fluids*, 25:071903, 2013.
- [105] U. Zimmermann, R. Schnettler, G. Klöck, and H. Watzka. Mechanisms of electrostimulated uptake of macromolecules into living cells. *Naturwissenschaften*, 77:543–545, 1990.